Observed Deep Cyclonic Eddies around Southern Greenland

SIJIA ZOU,[a,b] AMY S. BOWER,[b] HEATHER FUREY,[b] ROBERT S. PICKART,[b] LOÏC HOUPERT,[c] AND N. PENNY HOLLIDAY[c]

[a] *State Key Laboratory of Marine Environmental Science and College of Ocean and Earth Sciences, Xiamen University, Xiamen, China*
[b] *Woods Hole Oceanographic Institution, Woods Hole, Massachusetts*
[c] *National Oceanography Centre, Southampton, United Kingdom*

(Manuscript received 19 November 2020, in final form 4 August 2021)

ABSTRACT: Recent mooring measurements from the Overturning in the Subpolar North Atlantic Program have revealed abundant cyclonic eddies at both sides of Cape Farewell, the southern tip of Greenland. In this study, we present further observational evidence, from both Eulerian and Lagrangian perspectives, of deep cyclonic eddies with intense rotation ($\zeta/f > 1$) around southern Greenland and into the Labrador Sea. Most of the observed cyclones exhibit strongest rotation below the surface at 700–1000 dbar, where maximum azimuthal velocities are ~30 cm s^{-1} at radii of ~10 km, with rotational periods of 2–3 days. The cyclonic rotation can extend to the deep overflow water layer (below 1800 dbar), albeit with weaker azimuthal velocities (~10 cm s^{-1}) and longer rotational periods of about one week. Within the middepth rotation cores, the cyclones are in near solid-body rotation and have the potential to trap and transport water. The first high-resolution hydrographic transect across such a cyclone indicates that it is characterized by a local (both vertically and horizontally) potential vorticity maximum in its middepth core and cold, fresh anomalies in the deep overflow water layer, suggesting its source as the Denmark Strait outflow. Additionally, the propagation and evolution of the cyclonic eddies are illustrated with deep Lagrangian floats, including their detachments from the boundary currents to the basin interior. Taken together, the combined Eulerian and Lagrangian observations have provided new insights on the boundary current variability and boundary–interior exchange over a geographically large scale near southern Greenland, calling for further investigations on the (sub)mesoscale dynamics in the region.

KEYWORDS: North Atlantic Ocean; Cyclogenesis/cyclolysis; Lagrangian circulation/transport; Mesoscale processes; Ocean circulation

1. Introduction

Denmark Strait is one of the two major gateways for waters from the Nordic seas to flow into the North Atlantic (Fig. 1). These waters are highly stratified due to the large vertical range in salinity, and their outflow pathways are strongly density dependent (Bruce 1995; Spall and Price 1998). Downstream of the sill, waters with lighter densities are advected southwestward by the East Greenland Current (EGC). The denser waters descend the continental slope with increasing volume transport and decreasing density due to vigorous mixing and entrainment with the ambient subpolar waters (Price and Baringer 1994; Rudels et al. 2002; Girton and Sanford 2003; Lauderdale et al. 2008; Koszalka et al. 2017; North et al. 2018). While the product of the source and entrained water has decreased density, it constitutes the densest North Atlantic Deep Water—the Denmark Strait Overflow Water (DSOW), which feeds into the lower limb of the global meridional overturning circulation (Dickson et al. 2008). The DSOW spreads southwestward in the deep western boundary current (DWBC) underlying the EGC (Dickson et al. 2008; Bacon and Saunders 2010; Hopkins et al. 2019). By the time the boundary currents reach Cape Farewell, the southern tip of Greenland, a proportion is retroflected into the central Irminger Sea (Holliday et al. 2007). The remaining boundary currents turn around the tip and enter the Labrador Sea, where they flow northwestward with the DWBC overlaid by the West Greenland Current (Fig. 1; Dickson et al. 2008; Fischer et al. 2015; Pacini et al. 2020).

An important consequence of the dense water descent southwest of the Denmark Strait is the production of cyclonic (counterclockwise) eddies (Bruce 1995; Krauss 1996; von Appen et al. 2014). Numerical studies have proposed several possible formation mechanisms for these cyclones, including vortex stretching associated with the descent (Krauss and Käse 1998; Spall and Price 1998), bottom friction effects (Hill 1996), a combination of vortex stretching and friction (Käse et al. 2003), and baroclinic instability of the overflow plume current (Smith 1976; Swaters 1991; Jungclaus et al. 2001). Recent work suggests that the cyclones are connected to time-dependent variability in the dense overflow at the sill (von Appen et al. 2017; Almansi et al. 2020). The characteristics, propagation, and dissipation of these Denmark Strait overflow cyclones (DSOCs), together with other types of mesoscale variability, play a critical role in modifying the property, transport, and stability of the boundary current system (Bruce 1995; Krauss and Käse 1998; Jungclaus et al. 2001; Girton and Sanford 2003; Voet and Quadfasel 2010; Magaldi et al. 2011; Schaffer et al. 2016).

Using satellite infrared imagery and drifters, energetic cyclones with cold surface anomalies were observed to propagate

Corresponding author: Sijia Zou, sijiazou2018@gmail.com

DOI: 10.1175/JPO-D-20-0288.1

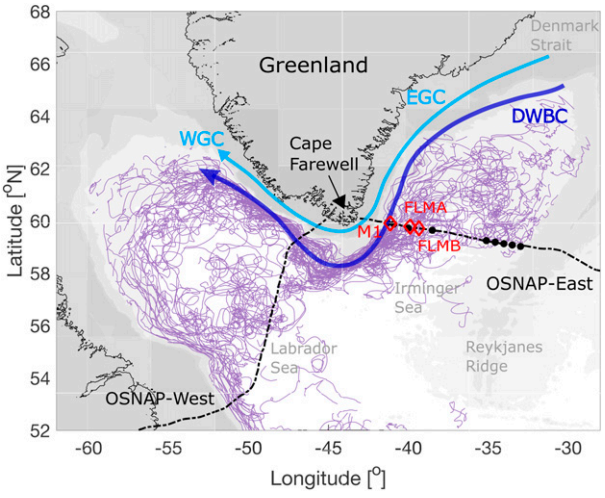

FIG. 1. Schematic of the boundary currents around Greenland. The shelfbreak East Greenland Current (EGC) and West Greenland Current (WGC) are shown in light blue. The deep western boundary current (DWBC) is shown in dark blue. The OSNAP-West and OSNAP-East sections are indicated as black dashed lines. Locations of moorings M1, FLMA, and FLMB are indicated as red diamonds. Launch locations of the 50 RAFOS floats are shown as black circles; 35 of them were launched in the DWBC east of Greenland, and 15 were launched along the western flank of the Reykjanes Ridge. The float trajectories are plotted in purple.

along the east Greenland shelf and slope from southwest of the Denmark Strait to ~63°N (Bruce 1995; Krauss 1996; Jungclaus et al. 2001). The estimated radii of the cyclones were 10–20 km and the azimuthal velocities were 20–40 cm s^{-1} (Table 1). These estimates are consistent with those based on a composite cyclone, which was constructed with mooring measurements across the east Greenland slope at 65.5°N (von Appen et al. 2014). The translational velocities of DSOCs were 20–72 cm s^{-1}, which was attributed to a combination of the advective velocity of the mean current and the self-propagating velocity expected from topographic Rossby waves and eddy dynamics (Krauss 1996; von Appen et al. 2014).

The vertical structure of the composite cyclone was also presented in von Appen et al. (2014). Cyclonic rotation was observed throughout the water column. The strongest circulation was located in the upper to intermediate layers (100–300 m), rather than in the deep overflow layer where isopycnals were significantly domed. Using an idealized model, Spall and Price (1998) found that the strong rotation above the overflow layer resulted from intensified midlevel stretching when the Denmark Strait outflow of high potential vorticity (PV) was advected into the low PV environment (i.e., the Irminger Sea). The role of the descending overflow water is to provide an along-slope density gradient balanced by a vertical shear in the offshore geostrophic velocity, allowing downgradient PV advection to occur.

Studies of the DSOCs have focused on the east Greenland continental slope immediately southwest of the Denmark Strait, where most observations are available. Questions remain about their downstream evolution and their potential influence on the boundary currents. Using a moored current meter array, Bacon and Saunders (2010) studied deep water transport variability during 2005/06 at southeastern Cape Farewell. They reported no predominance for cyclonic or anticyclonic rotation in the layer below 1500 m, suggesting a potential decay of the DSOCs by the time they reach this latitude. However, recent mooring observations from the Overturning in the Subpolar North Atlantic Program (OSNAP; Lozier et al. 2017) have revealed the presence of abundant DSOCs within the boundary currents on both sides of Cape Farewell, but smaller and slower than those observed near the Denmark Strait (Pacini et al. 2021). While Pacini et al. (2021) document the occurrence statistics and transport of the DSOCs, here we use a combination of Lagrangian floats, hydrographic measurements, and moorings from OSNAP-East to further understand the propagation, rotational characteristics, properties, and vertical structures of the cyclones around southern Greenland.

2. Data and methods

a. *RAFOS floats*

A RAFOS (range and fixing of sound) float is an acoustically tracked, isobaric drifter (Rossby et al. 1986). While drifting underwater, the float listens for and records acoustic signals from predeployed sound source moorings. Each float's position is calculated from these recorded signals, the sound source locations, and the speed of sound in water. The float also carries sensors to measure temperature and pressure at fixed time intervals.

In this study, we use data from 50 of the 125 isobaric RAFOS floats that were drifting in the western subpolar North Atlantic

TABLE 1. A summary of DSOC characteristics from previous observational studies. Frequency refers to the time elapsed between two cyclones at a fixed location. N/A = not available.

	Approach	Location	Radius (km)	Azimuthal velocity (cm s^{-1})	Rotational period (days)	Translation velocity (cm s^{-1})	Frequency (days)
Bruce (1995)	IR imagery	66°–63°N	10–20	N/A	N/A	20–30	2–3
Krauss (1996)[a]	Drifter	65°–63°N	10–15	20–40	1–3	30–50	N/A
von Appen et al. (2014)	Mooring	65.5°N	7.8	22	2–3	72	2.1

[a] The eddy characteristics reported here from Krauss (1996) are only for one of the three cyclones, which is referred to as "eddy A" in the study. The drifter trajectory trapped in this cyclone was long enough and thus yielded a more robust estimate on the cyclone's radius, period, etc.

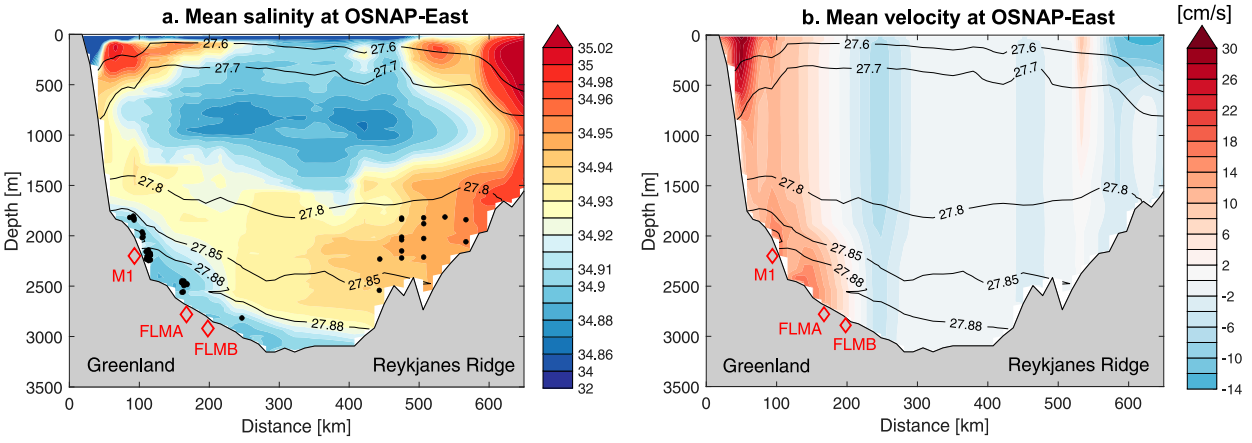

FIG. 2. (a) Mean salinity averaged over 21 months between August 2014 and April 2016 along the OSNAP-East section. Mean isopycnals are contoured in black. Black dots indicate the launch locations of the RAFOS floats used in this study. Locations of moorings M1, FLMA, and FLMB are indicated as red diamonds. (b) Mean velocity perpendicular to the OSNAP-East section. Positive (negative) values indicate southwestward (northeastward) velocities. Data used for these plots are the OSNAP gridded products, which used direct mooring observations within the boundary currents east of Greenland and west of the Reykjanes Ridge. More details are described in Lozier et al. (2019).

during 2014–18 (Ramsey et al. 2020). The floats were released along the OSNAP-East line, with 35 floats deployed in the DWBC east of Greenland and the others along the western flank of the Reykjanes Ridge (Fig. 1). The vertical float launch locations are shown in Fig. 2a, overlain on the mean salinity field along OSNAP-East. Floats were released at ~1800 dbar or deeper in the overflow water layer, whose density is generally greater than 27.80 kg m^{-3} (Dickson and Brown 1994). The 35 floats east of Greenland were released in both the DSOW layer (≥27.88 kg m^{-3}) and the Northeast Atlantic Deep Water (NEADW) layer (27.80–27.88 kg m^{-3}; Hopkins et al. 2019). The 15 floats west of the Reykjanes Ridge were launched in the salty NEADW layer (Fig. 2a). Note that since the RAFOS floats are isobaric, they approximately follow water parcel trajectories. The sample rate of temperature, pressure and location was set to 24 h and the maximum record length was 2 years. The sample rate is not ideal for short-period cyclone observation: the OSNAP float experiment was designed to measure large-scale spreading pathways, not necessarily the small, rapidly rotating eddies. Along-track velocity is calculated by differentiating between positions 48 h apart. Data are quality controlled and calibrated before analysis (Ramsey et al. 2020).

Note that some trajectory data are missing in the northeasternmost area of the Irminger Sea and the northwesternmost area of the Labrador Sea, where floats are far from the sound sources and cannot receive good quality sound signals, especially in winter (Ramsey et al. 2020). Here we only focus on the trajectories in the vicinity of Cape Farewell, where sound source signal reception and tracking were most robust.

1) IDENTIFYING LOOPING TRAJECTORIES FROM FLOAT DATA

Floats' velocities are highly variable on daily to weekly time scales (more in section 3b). The high-frequency variability originates from the eddy field, the along-track changes in topography, tracking uncertainties, and other unknown noise. To extract the eddy information, we identify each individual trajectory that contains a visually apparent loop that is likely associated with an eddy. At locations with strong background advection, such as southeast of Cape Farewell (section 3a), the trajectory of a float that follows an eddy may not trace out closed loop but cusps instead. In addition, in the absence of an apparent loop or cusp, along-track temperature is used to identify a potential eddy trajectory segment. A common feature for many apparent cyclonic loops/cusps is an increase and subsequent decrease of temperature near their apexes. This is because that while looping, the float following an isobar will cross the isotherms (or isopycnals) which tilt upslope toward the coast (Fig. 2). As a result, the float's temperature increases when it travels offshore and decreases when it travels onshore. The opposite is true for anticyclonic loops/cusps.

We record the date at the apex of each loop, cusp, and localized temperature anomaly (at least 0.5°C) as the time center and extract a 15-day track segment, with 7 days before and after the time center. The segment is referred to as a "looping trajectory." Note that more than one loop/cusp may be present in a looping trajectory. Sign of rotation (positive for cyclone and negative for anticyclone) associated with each looping trajectory is also recorded.

2) CALCULATING ADVECTIVE VELOCITY OF THE MEAN FLOW

By excluding looping trajectories from the set of all trajectories, we derive nonlooping trajectory segments that are used to compute the advective velocity of the mean flow below 1800 dbar. To derive a statistical mean and standard error of the velocity field, we divide the boundary current pathways into 34 regions. In each region, at least 20 velocity measurements are present (number of floats in each region may be smaller than 20) and topography features, such as topographic slope and curvature, are relatively uniform. In the ith region, where number of measurements is N_i, we randomly select $N_i/3$ measurements and average them to obtain $\mathbf{v}_i$. We repeat this

TABLE 2. CTD (MicroCAT) and current meter (CM) instrument depths at moorings M1, FLMA, and FLMB. The depths are slightly different between years.

M1	MicroCAT	50, 290, 520, 760, 1010, 1240, 1490, 1730, 1950 m
	CM	40, 520, 1000, 1480, 1720 m
FLMA	MicroCAT	15, 30, 50, 80, 120, 170, 240, 340, 500, 750, 1000, 1500, 1700, 2000, 2300, 2600 m
	CM	1700, 2000, 2330, 2650 m
FLMB	MicroCAT	30, 40, 60, 90, 130, 180, 250, 350, 500, 750, 1000, 1500, 1850, 2100, 2450, 2760 m
	CM	1800, 2100, 2500, 2760 m

process for 1000 times and derive the mean velocity for this region as $\bar{\mathbf{v}}_i = (1/1000)\sum_1^{1000}\mathbf{v}_t$. The associated standard error (SE) is estimated as

$$\mathrm{SE}_i = \sqrt{\frac{\sum(\mathbf{v}_t - \bar{\mathbf{v}}_i)2}{1000}}. \quad (1)$$

3) CALCULATING LOOPING CHARACTERISTICS WITH THE LEAST SQUARES METHOD

The characteristics of each looping trajectory are calculated using the least squares method (LSM; Armi et al. 1989; Richardson et al. 1989). Before applying LSM, we first filter the velocity time series of each trajectory with a fifth-order Butterworth bandpass filter with cutoff periods of 3–15 days. The bandpass-filtered velocity is considered as eddy velocity $\mathbf{v}_{\mathrm{eddy}}$, which is further decomposed into along-stream (unit vector: $\mathbf{l}$) and cross-stream (unit vector: $\mathbf{n}$) components. The low-pass-filtered (i.e., periods longer than 15 days) velocity in along-stream direction is used to approximate the translational velocity of the cyclone, which includes the background advective velocity and eddy self-propagating velocity. The high-pass-filtered velocities (i.e., periods shorter than 3 days) are considered as noise. Note that the LSM is applied to floats sampling the overflow water layer, where the cyclones' azimuthal velocities are relatively small and the rotational periods are relatively long (about a week). Therefore, the 3-day cutoff period is appropriate for this deep layer even though faster rotation at middepths may exhibit period shorter than 3 days (to be shown in section 4a).

LSM is applied to $\mathbf{v}_{\mathrm{eddy}}(t)$, the goal of which is to find the minimum of the sum of residuals $\sum R_t$. The residual R_t takes the form

$$R_t = \mathbf{v}_{\mathrm{eddy}} \cdot \mathbf{l} + i\mathbf{v}_{\mathrm{eddy}} \cdot \mathbf{n} - f(t, A, \omega),$$
$$\text{where} \quad f(t, A, \omega) = A_1 e^{\omega t i} + A_2. \quad (2)$$

The term $f(t, A, \omega)$ is the model function for the oscillatory signals, where A_1 represents amplitude (e.g., maximum azimuthal velocity), ω is angular frequency (1 day^{-1}), and A_2 is a constant. The looping characteristics can be further derived, including the looping azimuthal velocity $V_{\mathrm{azi}} = A_1$, looping period $T = 2\pi/\omega$, looping radius $R = V_{\mathrm{azi}}/\omega$, and the looping Rossby number $R_o = V_{\mathrm{azi}}/fR$.

For some looping trajectories, the minimum of $\sum R_t$ is still large because the universal cutoff period of 3–15 days does not always work well, especially for large loops whose looping periods are greater than 15 days. In those cases, we reset the cutoff period upper bound to $3 \times T$ days and repeat the LSM calculation until the best fit is found, i.e., when minimum of $\sum R_t$ stops decreasing.

b. Hydrographic section

In addition to the float data, we use observations from a hydrographic transect east of Greenland along the OSNAP-East line. The transect includes 30 conductivity–temperature–depth (CTD) casts that were conducted from 7 to 12 August 2014. The data were collected with a Sea-Bird 911+ instrument and bottle samples were taken to calibrate conductivity. Accuracies are 0.001°C for temperature, and 0.002 for salinity. The distance between the CTD stations ranges from 3 km near the Greenland coast to 40 km in the basin interior.

Absolute geostrophic velocity is calculated with reference to vessel-mounted acoustic Doppler current profiler (ADCP) velocity data in the upper 200 m (Lin et al. 2018). The ADCP velocity data were first detided with the Oregon State University TOPEX/Poseidon 1/12° Atlantic Ocean regional barotropic tidal model (Egbert and Erofeeva 2002) and gridded onto the locations of the CTD stations. The calculated absolute geostrophic velocity is perpendicular to the CTD section and is positive downstream (i.e., southwestward).

c. Moorings

Finally, we use August 2014–June 2018 time series from three tall moorings (M1, FLMA, and FLMB), situated between 2000- and 3000-m isobaths at OSNAP-East (Fig. 1). M1 is instrumented with nine Sea-Bird SBE37 MicroCATs, five current meters and an upward-facing bottom ADCP, providing property and velocity measurements throughout the water column (Table 2). Details of quality control and data calibration can be found in Hopkins et al. (2019). FLMA and FLMB are Ocean Observatories Initiative (OOI 2020) flanking moorings in the Irminger Sea. Both are instrumented with 14–16 MicroCATs throughout the water column and four current meters near the bottom (Table 2). Data records that exhibit significant salinity drifts or contain spikes (i.e., anomaly exceeds three times the standard deviation) are discarded.

All of the mooring velocity data are detided (Pawlowicz et al. 2002) and decomposed into along-stream ($\mathbf{l}$) and cross-stream ($\mathbf{n}$) components. The positive along-stream direction is selected as the direction following the depth-averaged mean current at each mooring (full depth-averaged at M1 and bottom layer-averaged at FLMA and FLMB). The cross-stream direction is 90° to the left of the along-stream direction and is therefore positive offshore. All profiles are

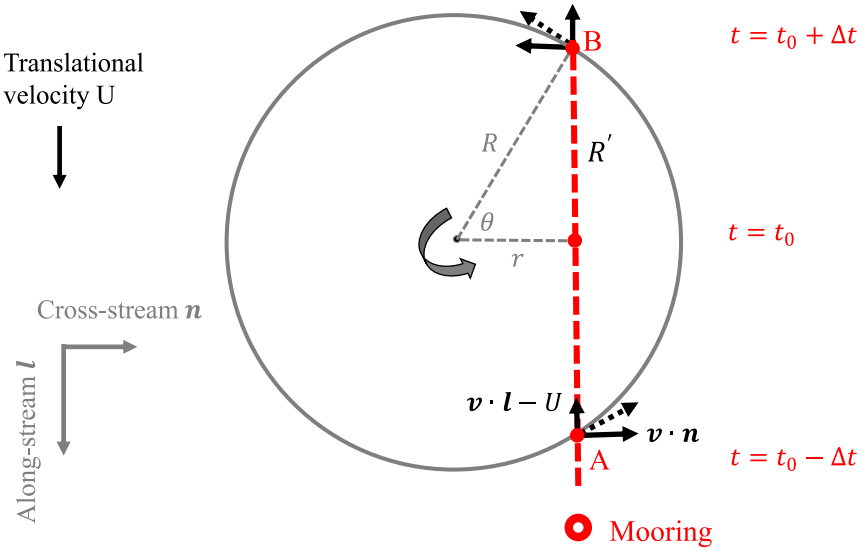

FIG. 3. Schematic of a mooring measuring a propagating cyclone along chord $\overline{AB}$ (red dashed line). Eddy translational velocity is U. At $t = t_0 - \Delta t$ ($t = t_0 + \Delta t$), the mooring intersects the cyclone at A (B), where along-stream velocity $\mathbf{v} \cdot \mathbf{l}$ and cross-stream velocity $\mathbf{v} \cdot \mathbf{n}$ are measured. The resultant along-stream velocity associated with the cyclone is $\mathbf{v} \cdot \mathbf{l} - U$; R' represents half distance between A and B.

linearly interpolated onto a 1-h grid in time and 50 dbar in the vertical.

d. *Calculating apparent eddy characteristics with a single mooring*

The distance between moorings is greater than 30 km, which is generally larger than the radii of the cyclones. As a result, we can only estimate the apparent eddy characteristics with individual mooring (Lilly and Rhines 2002; de Jong et al. 2014). Consider a Rankine vortex that is in solid-body rotation from the eddy center to a radius of R, beyond which the rotation decays exponentially. Most commonly, a mooring measures an ''apparent'' eddy along a chord $\overline{AB}$ over a time period of $2 \times \Delta t$ (Fig. 3; Lilly and Rhines 2002). The apparent eddy radius R' is estimated as half distance of $\overline{AB}$, i.e., $R' = U\Delta t$, where U is the eddy translational velocity. The apparent azimuthal velocity at R' is approximated as the cross-stream velocity at the intersections A and B, i.e., $V'_{\text{azi}} = (|\mathbf{v}_{t_0-\Delta t} \cdot \mathbf{n}| + |\mathbf{v}_{t_0+\Delta t} \cdot \mathbf{n}|)/2$, and the apparent rotational period is calculated as $T' = 2\pi R'/V'_{\text{azi}}$.

Compared to the actual eddy, the apparent eddy is generally smaller in size and weaker in rotation, except when the mooring crosses the eddy center. One simple way to examine whether the mooring cuts through the eddy center is to evaluate $r/R = \cos\theta = \{[|(\mathbf{v}_{t_0-\Delta t} \cdot \mathbf{l}) - U|/|\mathbf{v}_{t_0-\Delta t}|] + [|(\mathbf{v}_{t_0+\Delta t} \cdot \mathbf{l}) - U|/|\mathbf{v}_{t_0+\Delta t}|]\}/2$. If r/R is small, the mooring likely measures the eddy near its center and the above apparent estimates are more representative of the real values. If r/R is large and close to 1, the mooring likely crosses the eddy near its edge and the above apparent estimates are less representative. While we can derive the real eddy radius R with r/R and the apparent radius R', given the relatively large uncertainties of the derived U (section 4b) and the asymmetric magnitude between $\mathbf{v}_{t_0-\Delta t}$ and $\mathbf{v}_{t_0+\Delta t}$, we do not make any further corrections on R.

The terms t_0 and Δt are determined by maximizing the difference of the cross-stream velocity observed by the mooring, i.e.,

$$|\Delta\mathbf{v} \cdot \mathbf{n}| = |\mathbf{v}_{t_0+\Delta t} \cdot \mathbf{n} - \mathbf{v}_{t_0-\Delta t} \cdot \mathbf{n}|. \quad (3)$$

We derive the translational velocity U in two ways. For the first approach, U is simply defined as the background advective velocity U_{adv}, which is calculated as the mean velocity in the same month when the cyclone passed by, but excluding the time periods with the cyclone's presence (60 h before and 60 h after t_0). Another approach is to approximate U as the sum of U_{adv} and eddy self-propagating velocity U_{self}, the latter estimated from an analytical solution proposed by Nof (1983) (more details in section 4a).

3. Results from Lagrangian float data

a. *Mean advection measured by the RAFOS floats*

The regional mean and SE of the advective velocity magnitude around southern Greenland, derived from the nonlooping trajectories of the RAFOS floats, are shown in Fig. 4. Here we combine floats at all depths (≥1800 dbar) to yield statistically reliable estimates of the mean advection. The advective velocity is 4.6–22.5 cm s^{-1} around southern Greenland, with a mean of 15.7 cm s^{-1} (Fig. 4a). The strongest flow is observed southeast of the Eirik Ridge (~58.5°N, 43.0°–44.5°W) and west of Greenland between 60.0° and 61.5°N, where steep topographic slopes increase velocity to conserve transport between isobaths. The weakest flow is observed west of the

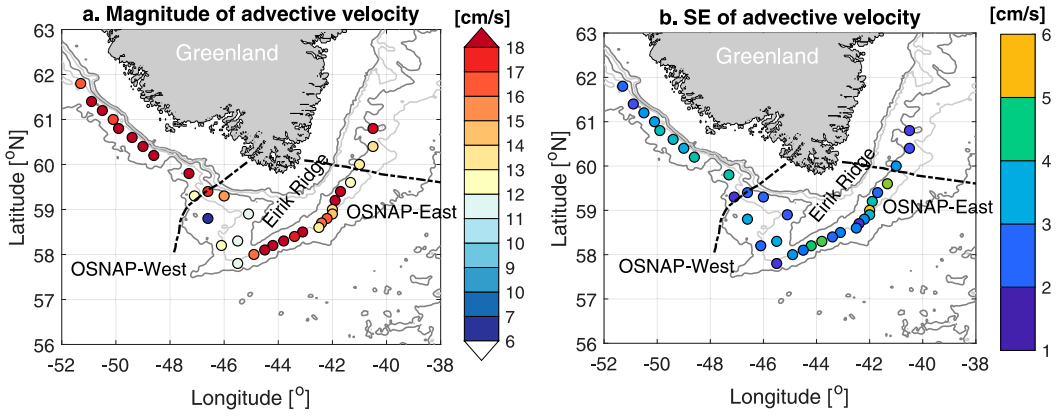

FIG. 4. (a) Mean advective velocity magnitude below 1800 dbar based on the nonlooping RAFOS float trajectories. (b) The standard error (SE) of the advective velocity magnitude. Isobaths of 1000, 2000, and 3000 m from ETOPO-2 are contoured as dark gray lines. Isobaths of 1500 and 2500 m are contoured as light gray lines. Unless noted otherwise, the bathymetric contours in the following figures are the same as those shown here.

Eirik Ridge (~58.8°N, 45.0°–47.0°W) where the topographic slope is weak. The SE of the mean advective velocity varies from 1.4 to 5.3 cm s^{-1} (Fig. 4b).

b. *Characteristics of cyclonic rotations observed by the RAFOS floats*

Looping float trajectories are observed throughout the boundary currents around southern Greenland (Fig. 5a). Both cyclonic and anticyclonic loops/cusps are present, with far more cyclonic (360) than anticyclonic (69). Some loops are found to detach from the boundary into the basin interior southwest of the Eirik Ridge and on both sides of Greenland, possibly enhancing boundary–interior exchange at these locations. We focus on the cyclonic loops/cusps within the boundary currents and derive their looping characteristics using LSM.

We start by describing the characteristics of three RAFOS floats (numbered 1307, 1308, and 1309) that were serendipitously launched in an intense DSOC evident in a hydrographic section (to be discussed in section 4a). The floats were released on 10 August 2014 at ~1820 dbar east of Greenland, where bottom depth is ~1900 m. After launch, they traveled along isobaths between 2000 and 3000 m around Eirik Ridge and into the Labrador Sea (Figs. 5b–d). During their southwest drift east of Eirik Ridge, all three floats showed consistent cyclonic loops/cusps in their trajectories. LSM is applied to the time series of eddy velocity for each looping trajectory (Fig. 6 for float 1307 as an example). The derived azimuthal velocity averaged over all looping trajectories is 10.0 cm s^{-1}, with a standard deviation (SD) of 3.2 cm s^{-1} (Table 3). The looping period is 5.8 ± 1.5 days, and the looping radius is 8.3 ± 3.8 km. The Rossby number is 0.11 ± 0.03, suggesting that nongeostrophic terms in the momentum balance are small but not negligible. The translational velocity is 13.4 ± 4.4 cm s^{-1}.

West of the Eirik Ridge, all three floats turned northward, but with very different looping behaviors (Figs. 5b–d). Float 1307 continued following a cyclonic eddy with looping characteristics similar to those east of the ridge, except for weaker translational velocity (0.3–3.4 cm s^{-1}; Fig. 6). On the contrary, float 1308 looped anticyclonically along its northward path. Float 1309 traced out a cyclonic cusp at 58.9°N west of the Eirik Ridge, likely resulting from the float passing around the small topographic feature with a closed 3000-m isobath. Further northwestward beyond Eirik Ridge, all three floats traveled along the boundary current for about a month without apparent looping until 60°–62°N, where 1309 drifted into the interior Labrador Sea and the other floats showed cyclonic cusps. It is not possible to ascertain the origin of these cyclonic cusps west of Greenland just based on the trajectories.

To obtain a statistical description of all looping trajectories, we extend the LSM analysis to all 50 RAFOS floats, that together exhibit 360 cyclonic loops/cusps around southern Greenland (Table 3). The averaged looping velocity is 7.6 cm s^{-1}, with a SD of 3.7 cm s^{-1}. The mean looping radius is 8.1 ± 4.4 km, and the mean looping period is 8.1 ± 2.9 days. The resultant Rossby number is 0.08 ± 0.03. The mean translational velocity is 9.0 cm s^{-1} with a large SD of 7.0 cm s^{-1}. This large SD results from the wide spread of the advective velocity among geographical locations.

Although some caution is advised when interpreting a single float trajectory with looping behaviors, the fact that the observed loops are predominantly cyclonic suggests that the floats are very likely measuring DSOCs, rather than unstable current and/or propagating waves that would involve rotations in both directions (i.e., cyclonic and anticyclonic; Smith 1976; Jiang and Garwood 1996; Regier and Stommel 1979). This is proven to be true at least for the three floats shown in Figs. 5b–d, which were serendipitously released in an identifiable DSOC observed by a hydrographic transect (section 4a).

Float trajectories provide matchless information on the evolution and pathways of the cyclones, but they represent the eddies only at one depth and at the radius of float looping. In the following sections, we use Eulerian observations to determine the horizontal and vertical structure of the cyclones.

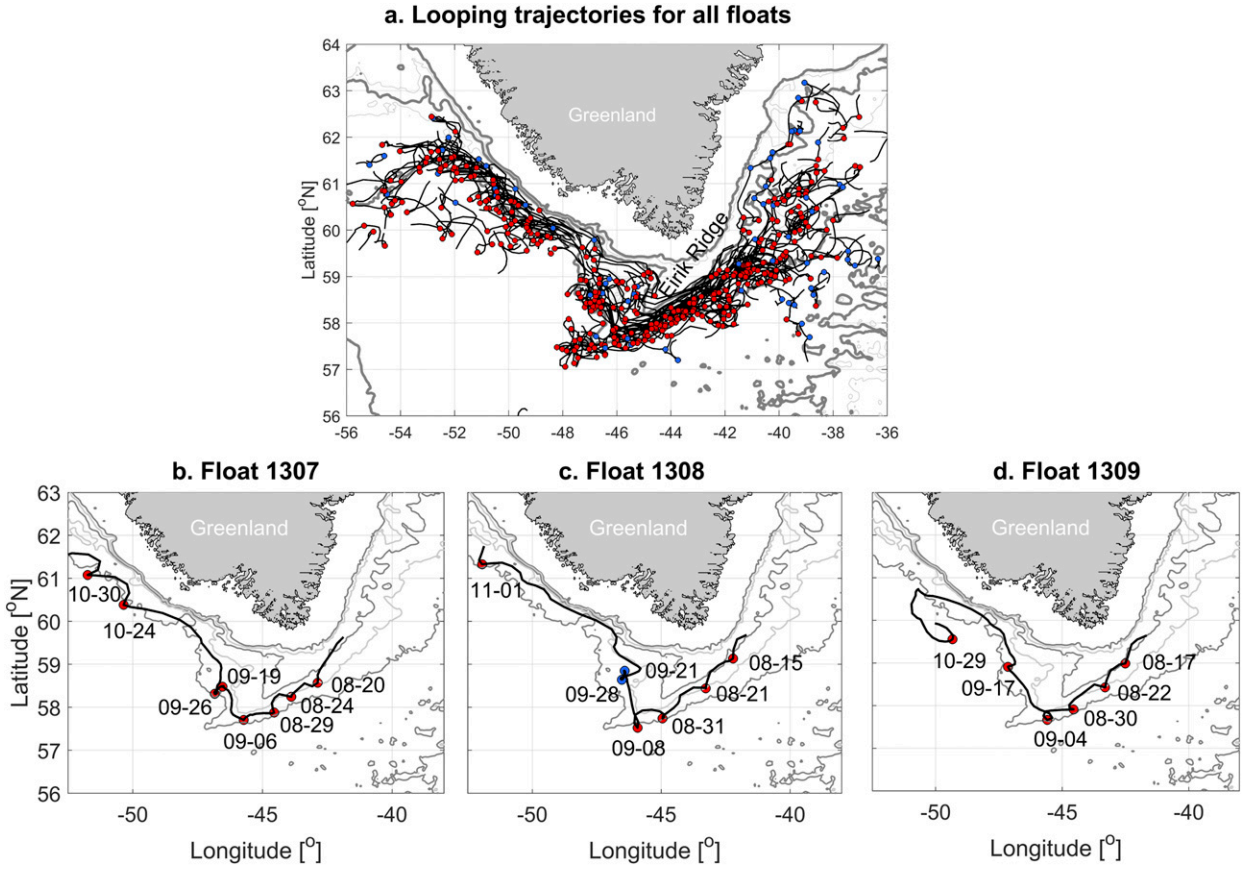

FIG. 5. (a) All looping trajectories of the RAFOS floats. The 15-day looping trajectories are plotted as black lines. Cyclonic loops/cusps are indicated as red circles and anticyclonic loops/cusps are indicated as blue circles. (b)–(d) Individual float trajectory and identified loops/cusps for float 1307, 1308, and 1309 that were released on 10 Aug 2014 at 59.9°N east of Greenland. The floats drifted at a pressure level of ~1820 dbar. The dates associated with the loops/cusps are labeled nearby as MM-DD.

4. Results from Eulerian data

a. *An intense cyclonic eddy observed in a hydrographic transect*

1) THE VELOCITY STRUCTURE

Vertical sections of potential temperature and salinity from a high-resolution hydrographic survey are shown in Fig. 7. At ~70 km from the Greenland coast, a pinching of isotherms, isohalines, and isopycnals toward the pressure level of ~800 dbar indicate the presence of a cyclonic eddy. The downward-deflected isolines in the upper 100–800 dbar result in warm, salty, and light anomalies compared to the ambient waters at the same pressure levels outside the eddy. In the layer below 1000 dbar, the domed isolines represent cold, fresh, and dense anomalies. Based on the calculated absolute geostrophic velocity fields, counterclockwise circulation is evident throughout the water column, with intensified rotation at ~800 dbar (Fig. 8a). Note that the velocity magnitude is not symmetric about the eddy center at ~70 km because the cyclone is embedded in a strong southwestward background flow.

The cyclone's translational velocity U can be approximated as the distance-averaged geostrophic velocity within the rotational diameter from 64 to 80 km (between dashed lines in Fig. 8a). The underlying assumption is that the U does not change significantly within this distance range. It contains both the advective velocity of the background flow and the eddy self-propagating velocity. The vertical profile of U is nearly barotropic (Fig. 8b), with a depth-averaged value of 21.0 cm s^{-1}. Below 1000 dbar, it slightly increases with depth, with a maximum of 24.3 cm s^{-1} reached at 1820 dbar.

To the lowest order, the cyclone is in geostrophic balance and its azimuthal geostrophic velocity v_{geo} may be calculated by subtracting the translational velocity U from the total absolute geostrophic velocity. However, provided that the Rossby number is not small (Table 3 and further shown below), we need to incorporate the centripetal acceleration into the geostrophic balance and derive the eddy velocity in gradient wind balance. In cylindrical coordinates, we have

$$\frac{v^2}{r} + fv = \frac{1}{\rho_0}\frac{\partial p}{\partial r}, \tag{4}$$

where r is the distance relative to the eddy center, v is the azimuthal velocity at r, and $(1/\rho_0)(\partial p/\partial r)$ is the pressure gradient force that is associated with the geostrophic component of the

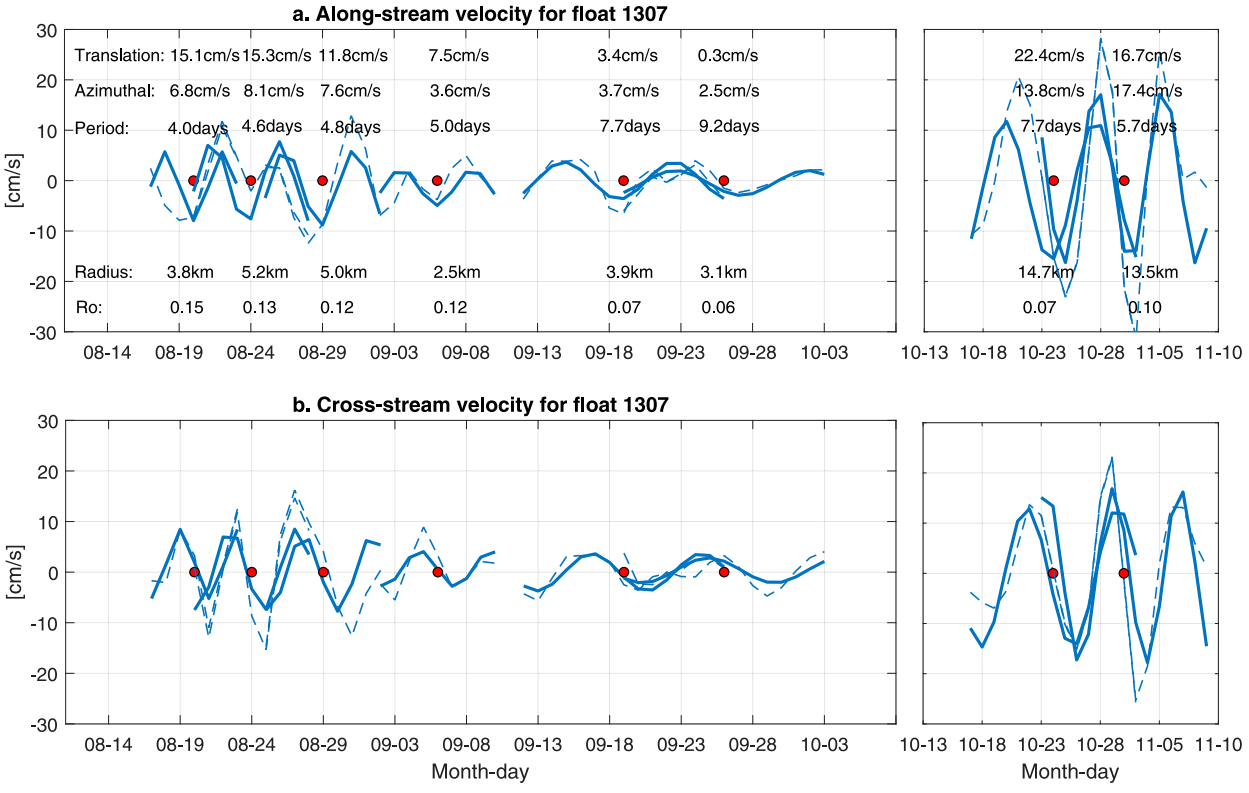

FIG. 6. Time series of eddy velocities in (a) along-stream and (b) cross-stream directions for float 1307. Each loop/cusp is indicated as a red circle. The original eddy velocity time series associated with each looping trajectory are plotted as dashed lines and the fitted velocity time series from LSM are plotted as solid lines. Both time series are $3 \times T$ days long, where T is the looping period. The derived looping characteristics for each looping trajectory are labeled.

eddy velocity, i.e., $fv_{\text{geo}}(r) = (1/\rho_0)[\partial p(r)/\partial r]$. Equation (4) can therefore be written as

$$\frac{v^2}{r} + fv - fv_{\text{geo}} = 0. \tag{5}$$

With known v_{geo} and r, we can solve for $v(r)$, which is further projected on to the local Cartesian coordinate as v_{eddy} (Fig. 9a). The relatively symmetric velocity structure reveals the eddy center located at 72 km in the horizontal. The cyclonic circulation is observed throughout the water column, with the strongest rotation reached between 700 and 1000 dbar. The distribution of the eddy velocity relative to the eddy center can be fitted by a Gaussian eddy model (e.g., von Appen et al. 2014)

$$v_G(n) = -V_{\text{azi}} \frac{n - n_0}{R} \exp\left[\frac{1 - \left(\frac{n - n_0}{R}\right)^2}{2}\right], \tag{6}$$

where $n - n_0$ is the distance n relative to the eddy center n_0. The V_{azi} is the magnitude of the maximum azimuthal velocity, and R is the radius at which V_{azi} is reached. In this model, when $|n - n_0| < R$, $|v_G|$ increases nearly linearly with $|n - n_0|$ and reaches its maximum at R. When $|n - n_0| > R$,

TABLE 3. Characteristics of the looping trajectories. The top four rows are for floats 1307, 1308, and 1309 and their averages east of the Eirik Ridge. The term N is the number of looping trajectories; $\overline{V_{\text{azi}}} \pm$ SD is the mean azimuthal velocity averaged over looping trajectories and its SD; $\overline{T} \pm$ SD is the mean looping period and its SD; $\overline{R} \pm$ SD is the mean looping radius and its SD; $\overline{R_o} \pm$ SD is the mean Rossby number and its SD; $\overline{U} \pm$ SD is the mean translational velocity and its SD. The bottom row in bold is based on the entire 50 floats around southern Greenland. Calculation methods can be found in section 2a.

Float	N	$\overline{V_{\text{azi}}} \pm$ SD (cm s^{-1})	$\overline{T} \pm$ SD (days)	$\overline{R} \pm$ SD (km)	$\overline{R_o} \pm$ SD	$\overline{U} \pm$ SD (cm s^{-1})
1307	4	6.5 ± 2.0	4.6 ± 0.4	4.1 ± 1.2	0.13 ± 0.01	12.4 ± 3.7
1308	4	12.1 ± 0.9	6.9 ± 1.0	11.5 ± 1.0	0.08 ± 0.02	13.8 ± 5.5
1309	4	11.3 ± 2.9	6.0 ± 1.8	9.4 ± 3.6	0.10 ± 0.04	14.1 ± 4.9
All 3	12	10.0 ± 3.2	5.8 ± 1.5	8.3 ± 3.8	0.11 ± 0.03	13.4 ± 4.4
All 50	**360**	**7.6 ± 3.7**	**8.1 ± 2.9**	**8.1 ± 4.4**	**0.08 ± 0.03**	**9.0 ± 7.0**

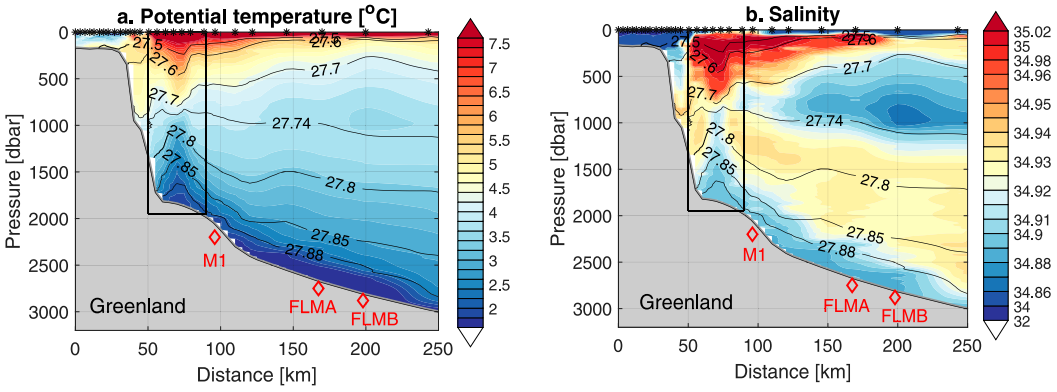

FIG. 7. Vertical sections of (a) potential temperature and (b) salinity for the CTD transect conducted during 7–12 Aug 2014. Potential density surfaces are contoured in black. The CTD station locations are indicated as black asterisks along the top. Red diamonds indicate locations of moorings M1, FLMA, and FLMB. The black box denotes the area where the cyclone is present.

$|v_G|$ decreases exponentially with $(n - n_0)^2$. Then we use LSM to find V_{azi}, R and n_0.

Figure 9b shows the vertically averaged eddy velocity between 700 and 1000 dbar, the levels with the strongest rotation, as a function of distance, together with a fitted curve based on the Gaussian eddy model. The good fit of the model suggests that the cyclone is in near solid-body rotation within the maximum azimuthal velocity according to the overall linear relationship between v_G and n. The estimated maximum azimuthal velocity V_{azi} is 37.0 cm s^{-1}, and the radius R is 8.0 km. The rotational period is therefore $T = 2\pi R/V_{azi} = 1.6$ day and the Rossby number is $R_o = (V_{azi}^2/R)/fV_{azi} = 0.37$.

The rotational characteristics derived from the full-depth hydrographic field are different from the looping characteristics based on the three RAFOS floats released in the deep overflow layer of the same cyclone (black dots in Fig. 9a), because the azimuthal speed is weaker there compared to the overlying layer. The rotational characteristics in the overflow layer (at 1800 dbar) from the hydrographic data give azimuthal velocity of ~11.6 cm s^{-1} at a radius of 8.0 km, with a rotational period of 5.3 days. These estimates are comparable to those based on the three RAFOS floats (Table 3; V_{azi} = 10.0 cm s^{-1}, R = 8.3 km, and T = 5.8 days). It is therefore suggested that the relatively weak cyclonic loops/cusps observed by the deep RAFOS floats are likely underlying

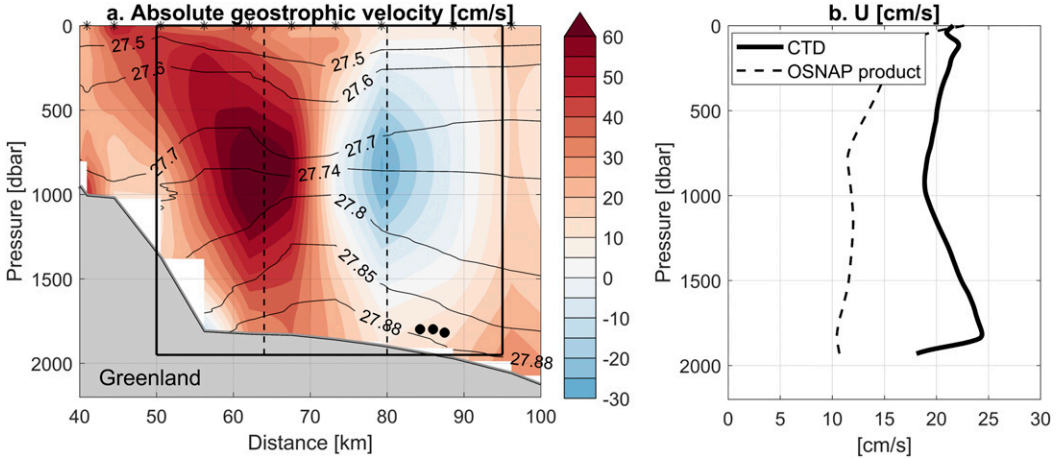

FIG. 8. (a) Vertical section of absolute geostrophic velocity for the CTD transect. Positive velocity is southwestward. Black asterisks along the top denote CTD station locations. The black box denotes the area where the cyclone is present. The release locations for RAFOS floats 1307, 1308, and 1309 are shown as black circles. (b) The vertical profile of the translational velocity U (black solid curve), which is calculated as the distance-averaged geostrophic velocity from 64 to 80 km [between the two dashed black lines in (a)]. Black dashed line represents the mean velocity profile that is averaged over the same distance from 17 to 31 Aug 2014, i.e., after the passage of the cyclone, based on the OSNAP mooring measurements.

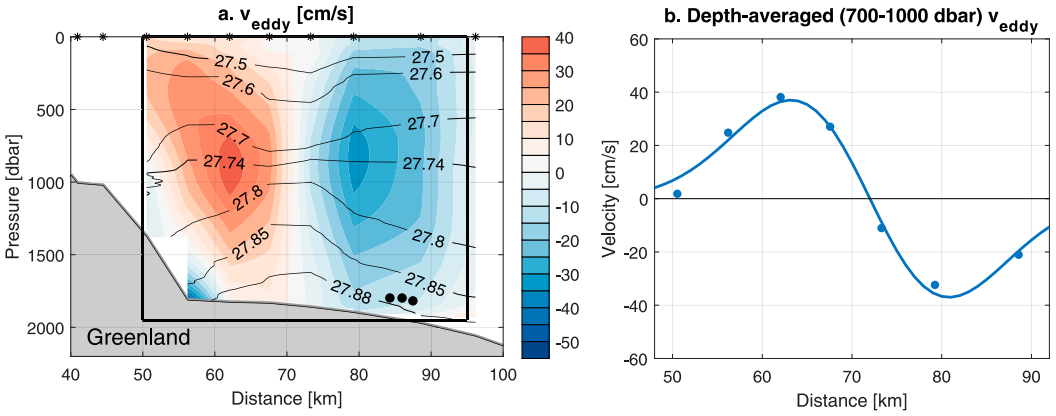

FIG. 9. (a) Eddy velocity in gradient wind balance (i.e., v_{eddy}). (b) The vertically averaged v_{eddy} between 700 and 1000 dbar as a function of distance. Blue dots indicate eddy velocities at each CTD station location. It is worth noting that the three casts between 64 and 80 km were conducted within several hours on the same day. Solid line represents the fitted curve from the Gaussian eddy model.

much stronger circulations at the intermediate depths above (consistent with Pacini et al. 2021).

2) FLUID TRAPPING AND THE SELF-PROPAGATING SPEED

One important characteristic of a propagating vortex or wave is that it may be able to trap fluid while traveling over a long distance. This in turn means that the cyclones have the potential to transport property anomalies to the boundary current and the ocean interior (if they detach from the boundary). The ability of fluid trapping is dependent upon the relative magnitudes of the azimuthal velocity V_{azi}, the phase speed c, and the background advective flow field U_{adv} (Flierl 1981; Regier and Stommel 1979), i.e.,

$$r_{trap} = \left| \frac{U_{adv} - c}{V_{azi}} \right|. \tag{7}$$

If the difference between the phase velocity and the background advective velocity is smaller than the azimuthal velocity in magnitude, i.e., $r_{trap} < 1$, then the vortex/wave may be able to trap fluid. For the CTD cyclone, the total translational velocity U, including U_{adv} and self-propagating velocity U_{self} (or c), is ~19.1 cm s^{-1} at 700–1000 dbar (Fig. 8b). Since both U_{adv} and U_{self} are in the downstream direction, the difference between the two should be smaller than 19.1 cm s^{-1} and therefore smaller than the maximum V_{azi}, which is 37.0 cm s^{-1} at the same depth (Fig. 9). This suggests that the cyclone is very likely to kinematically trap fluid within the middepth rotational core. More quantitatively, U_{adv} may be estimated with the OSNAP mooring-based daily velocity profiles averaged horizontally between 64 and 80 km and temporally during 17–31 August 2014 (after the passage of the cyclone). At 700–1000 dbar, U_{adv} is 11.6 cm s^{-1} (Fig. 8b) and U_{self}, estimated as the difference between U and U_{adv}, is 7.5 cm s^{-1}. The resultant r_{trap} is ~0.12 and the percentage of fluid contained in the trapping region of the cyclone is approximately 70%–90% of the entire cyclone, as suggested by results from a couple of kinematic models (Regier and Stommel 1979; Flierl 1981). Below the middepth rotational core, r_{trap} increases with decreasing azimuthal velocity, implying weaker capability of fluid trapping at depth. Nonetheless, the three floats released in the deep layer of the cyclone appear to be trapped because they show loops and cusps in their trajectories, which are typical characteristics for particles trapped in an eddy/wave (Regier and Stommel 1979).

The derived U_{self} of 7.5 cm s^{-1} is further compared with the analytical solution from Nof (1983). Using a two-layer analytical model, Nof (1983) found that, in the absence of friction, the self-propagating speed of an isolated vortex on a sloping bottom can be formulated as

$$c_{Nof} = \frac{g'}{f}\alpha, \tag{8}$$

where $g' = (\Delta\rho/\rho_0)g$ is reduced gravity and α is the topographic slope. The equation has been shown to well represent the propagating speed of baroclinic eddies on a sloping bottom based on laboratory experiments (e.g., Whitehead et al. 1990) and analytical solutions (Swaters and Flierl 1991). It is also consistent with propagating speeds of the DSOCs estimated from model simulations (Jungclaus et al. 2001) and mooring observations (von Appen et al. 2014). For the cyclone at the CTD section, g' is ~10^{-3} m s^{-2}, with $\Delta\rho$ between the overflow layer and the overlying layer of ~0.1 kg m^{-3}. The slope α is ~0.008, and the resultant c_{Nof} is 6.0 cm s^{-1}. While it remains questionable whether the Nof relationship is appropriate to describe the cyclone propagation (further discussed in section 5c), the comparable magnitudes between c_{Nof} and U_{self} derived above suggest that it may still be useful to provide a rough estimate on the self-propagating speed of the cyclone.

3) THE PV STRUCTURE

It is hypothesized that the cyclone observed at the CTD section is a DSOC, which is produced by vortex stretching when high PV outflow waters from Denmark Strait are injected

into the low PV Irminger Sea (Spall and Price 1998). With the potential to trap fluid, the DSOC likely carries the high PV anomalies while propagating downstream from the source. Here we examine the PV structure of the cyclone at the hydrographic section by calculating the Ertel PV, which is expressed as

$$\mathrm{PV} = -\frac{1}{\rho_0}(f\mathbf{k} + \boldsymbol{\zeta}) \cdot \nabla\rho. \tag{9}$$

The term $f\mathbf{k}$ is the planetary vorticity in the local vertical direction, and $\boldsymbol{\zeta}$ is the relative vorticity. In the axisymmetric cylindrical coordinates, the Ertel PV for an eddy in gradient wind balance takes the form

$$\mathrm{PV} = -\frac{f}{\rho_0}\frac{\partial\rho}{\partial z} - \frac{\zeta_z}{\rho_0}\frac{\partial\rho}{\partial z} - \frac{1}{g}\left(f + \frac{2v}{r}\right)\left(\frac{\partial v}{\partial z}\right)^2, \tag{10}$$

where $\zeta_z = (\partial v/\partial r) + (v/r)$ is the relative vorticity in the local vertical direction. The azimuthal velocity v is represented as $|v_{\mathrm{eddy}}|$. The last term on the right hand side is the horizontal component of the Ertel PV, which is one to two orders of magnitude smaller than the other two terms and is therefore neglected.

The total Ertel PV, shown in Fig. 10a, is high in the upper 300 dbar due to the strong stratification near the surface (Fig. 10b). Another significantly high PV core is observed at intermediate depths between 700 and 1100 dbar, where rotation is the most intense. While PV-f, denoting $-(f/\rho_0)\partial\rho/\partial z$, explains a significant amount of this high PV core (Fig. 10b), the contribution from the relative vorticity is equally important (Fig. 10c). Specifically, ζ_z/f is greater than 1 within the rotational core at 830 dbar. Outside of the cyclone, the total PV is primarily determined by PV-f (not shown).

The large ζ_z/f and high PV within the rotation core are consistent with the hypothesis that the cyclone is formed by vortex stretching during the outflow descent south of Denmark Strait. The intensified rotation is located in the layer of 27.70–27.80 kg m^{-3}, which was shown to be the layer with the most prominent stretching during the descent by previous studies (Ross 1982; Spall and Price 1998). It is acknowledged that these studies are based on the assumption of a steady outflow through the Denmark Strait, whereas recent observations have shown that the outflow is highly variable with rotations in both directions (von Appen et al. 2017; Spall et al. 2019; Lin et al. 2020). Nevertheless, despite the different initial rotation at the sill, a modeling study suggests that positive ζ_z can be developed/reinforced by vortex stretching downstream of the sill (Almansi et al. 2020), which is consistent with the observations of von Appen et al. (2017). At some distance south of the sill, the resultant strong rotation makes the cyclone capable of trapping the high stratification outflow waters (compared to the ambient waters in the Irminger Sea) along propagation.

4) WATER PROPERTIES

As stated above, the potential of the DSOC to trap fluid suggests that it may introduce property anomalies to the boundary current and ocean interior (if it detaches from the boundary current). Figure 11a shows the potential temperature–salinity (θ–S) profiles within the CTD cyclone. They are further compared with the daily θ–S profiles in the same month but during days after the cyclone's passage, i.e., from 17 to 31 August 2014. These profiles are referred to as the monthly background.

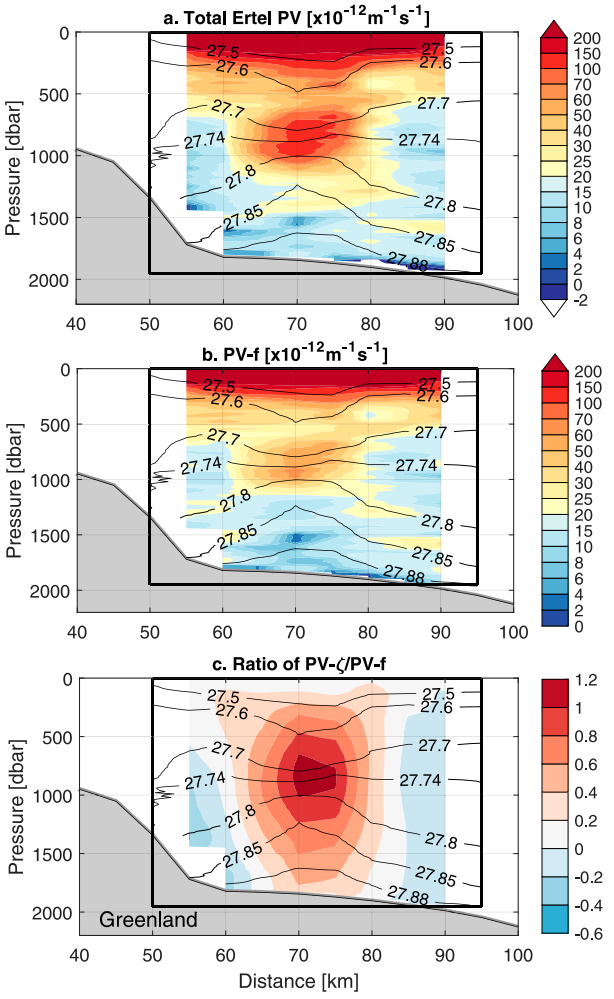

FIG. 10. (a) Total Ertel PV within the cyclone. (b) The stretching term PV-f $[-(f/\rho_0)(\partial\rho/\partial z)]$. (c) The ratio of relative vorticity ζ_z and planetary vorticity f, i.e., ζ_z/f. In all plots, the data are smoothed vertically with a 100-dbar running window to reduce noise.

The property anomalies introduced by the cyclone passage vary by density class. In the layer lighter than 27.65 kg m^{-3}, the cyclone contains warmer and saltier waters compared to the monthly background. In the layer denser than 27.74 kg m^{-3}, especially in the 27.74–27.85 kg m^{-3} layer, the cyclone contains cold and fresh anomalies, whose values are consistent with those southwest of the Denmark Strait in the same density layer (not shown). In addition, the cyclone introduces dense anomalies by having a bottom density greater than 27.88 kg m^{-3}, which is the maximum density of the monthly mean background. It should be noted that the cyclone passage is not the only cause of the dense anomalies

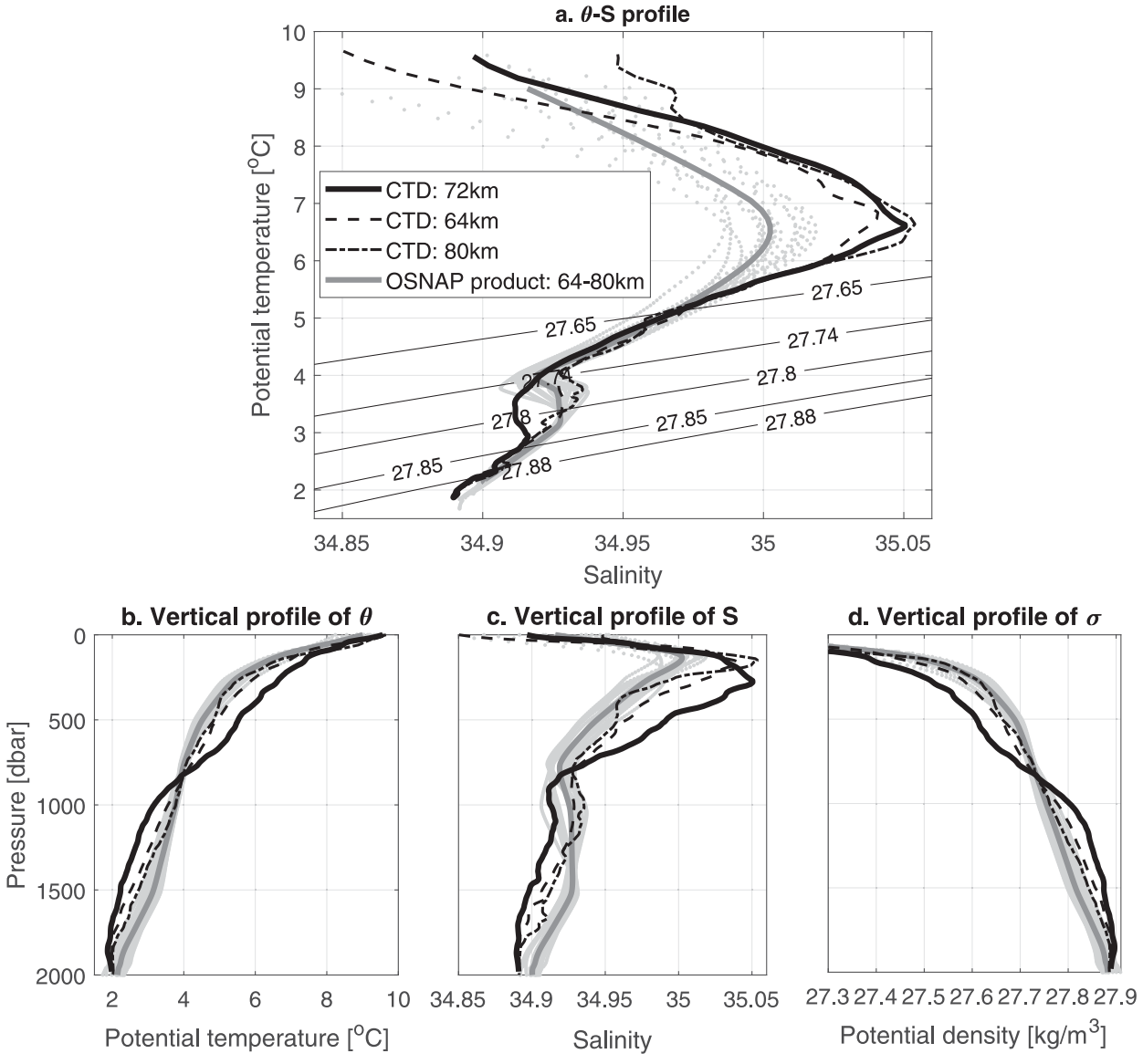

FIG. 11. (a) θ–S profiles and (b)–(d) vertical profiles associated with the cyclone at the CTD transect in August 2014. The profiles at the eddy center (i.e., at 72 km from coast) are plotted as black solid lines. The profiles at the maximum velocity radii (i.e., at 64 and 80 km from coast) are plotted as black dashed lines. Gray curves/dots represent the profiles averaged between 64 and 80 km based on OSNAP mooring measurements: the dots denote the daily profiles from 17 to 31 Aug 2014 and the curves are the temporal mean during this period.

because other daily profiles show the presence of similar density anomalies.

Over the bulk of the density layer $\geq 27.65\,\mathrm{kg\,m^{-3}}$, the θ–S difference between the cyclone and the monthly background decreases from the eddy center to the edges, suggesting increased mixing ratio of the cyclone to ambient waters and decreased kinematic trapping from the center of the cyclone outward. The mixing with the ambient waters is also evident from the vertical profiles of the properties shown in Figs. 11b–d. The center of the cyclone is characterized by relatively strong vertical gradients of temperature, salinity, and density, whereas at the radii of maximum azimuthal velocities, the vertical gradients are much weaker and are more similar to the background profiles.

b. *Cyclonic eddies observed by the moorings*

To extend the information about the cyclone characteristics to a larger temporal domain, we use hourly observations during August 2014 and June 2018 from three moorings, M1, FLMA and FLMB. These moorings span the regions where the RAFOS floats drifted by. A potential DSOC is identified when there is (i) a subsurface positive PV anomaly; (ii) doming isopycnals near the bottom; and (iii) a strong cross-stream velocity reversal that extends

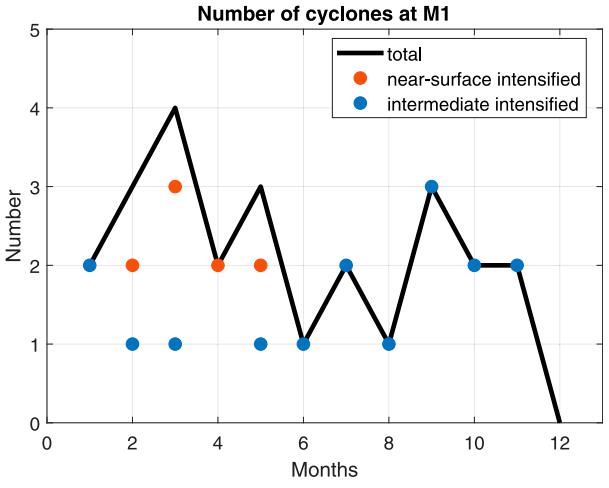

FIG. 12. Number of identified cyclones during August 2014–June 2018 as a function of month at mooring M1. Black line represents the total number of cyclones in each month. The orange (blue) dot represents the number of cyclones whose intense rotation is located in the near-surface (intermediate) layer.

down to the bottom layer. With the above criteria, surface-intensified eddies (cyclones or anticyclones), dipoles and other mesoscale variations without bottom expression are excluded.

1) THE CHARACTERISTICS

During the 4-yr time period, 25 cyclones are observed by mooring M1. At least one cyclone passed by the mooring in each month except in December (Fig. 12). The derived mean characteristics of the cyclones are summarized in Table 4. The duration times of the cyclones at M1 range from 14 to 76 h, with a mean of 36 h and a SD of 18 h. The total duration time summed among all passing cyclones is 38 days (916 h), accounting for about 3% of the 4-yr mooring record. The apparent azimuthal velocity at the intense rotation core varies between 9.9 and 52.4 cm s^{-1} among cyclones, with a mean of 28.2 ± 9.4 cm s^{-1}. The mean advective velocity U_{adv} is 10.4 ± 3.2 cm s^{-1}. If the eddy self-propagating velocity is not considered and U_{adv} is used to approximate the total translational speed (i.e., $U = U_{adv}$), the derived apparent radius R' is 6.4 ± 3.0 km, and the apparent rotational period T' is 1.8 ± 1.0 days. The associated Rossby number is 0.43 ± 0.27.

However, in addition to U_{adv}, the cyclone may also self-propagate at an appreciable speed U_{self}, which is estimated with the Nof solution given by Eq. (8). The calculated U_{self} is 5.9–7.7 cm s^{-1} given that $\Delta\rho$ varies from 0.10 to 0.14 among the 25 cyclones. As such, the mean translational velocity $U = U_{adv} + U_{self}$ becomes 16.8 ± 3.4 cm s^{-1} among the cyclones (Table 4). The mean apparent radius R' is 10.6 ± 4.7 km, and the rotational period T' becomes 3.0 ± 1.6 days. The associated Rossby number is 0.26 ± 0.16. For both sets of U, the mean ratio of r/R is 0.4–0.5, indicating that on average, the mooring cuts through the cyclone at the middle point between the eddy center and its edge at R. Finally, compared to the rotation core, the azimuthal velocity in the overflow water layer (below 1800 dbar) is weaker (13.5 ± 5.7 cm s^{-1}) and the associated rotational period is longer, which is 4.3 ± 3.1 days with $U = U_{adv}$ and 7.0 ± 4.9 days with $U = U_{adv} + U_{self}$.

For most of the cyclones at M1 (18/25), the along-stream velocity anomalies at the apparent eddy center are negative. This suggests that the eddy centers passed to the west (inshore) of M1, which is confirmed by observations with inshore moorings by Pacini et al. (2021). We thus expect fewer cyclone occurrences offshore at moorings FLMA and FLMB. During the 4-yr observational records, only one cyclone, identified by the uplifted isopycnals and cross-stream velocity reversal in the bottom, is observed at FLMB in September 2017.

2) THE VERTICAL STRUCTURE

Of the 25 cyclones observed at mooring M1, 16 of them exhibit vertical structures similar to that of the CTD cyclone, with intensified rotation and high stratification at intermediate depths (700–1200 dbar; Figs. 13a,b). The other 9, however, have the strongest rotation at depths shallower than 500 m. An example is shown in Fig. 13d, where a surface-intensified cyclone of strong azimuthal velocity (52.5 cm s^{-1}) is observed on 7 March 2015. Uplifted isopycnals extend from bottom to near-surface, introducing positive density anomalies throughout the water column. The positive stratification anomaly within the cyclone is also shifted upward to above 500 m (Fig. 13e).

The dynamic pressure associated with the cyclone can be constructed by integrating the gradient wind Eq. (4) radially,

$$p = \rho_0 \int_{-\infty}^{r} \frac{v^2}{r'} + fv\, dr'. \tag{11}$$

Parameter p is negative throughout the water column within the cyclone, and the depth of minimum p is collocated with the

TABLE 4. The mean and SD of apparent eddy characteristics for the 25 cyclones observed at mooring M1. The term Δt: half duration of the cyclone at the mooring (hours); V'_{azi}: apparent azimuthal velocity; U_{adv}: advective velocity; U_{self}: eddy self-propagating velocity that is approximated with the Nof formula; U: translational velocity; R': apparent radius; T': apparent rational period; r/R: the ratio measuring the mooring position relative to eddy center; and R_o: Rossby number. Note that we report two sets of R', T', r/R, and R_o depending on how we define U. For the first set, U is defined as U_{adv}. For the second set, U is defined as the sum of U_{adv} and U_{self}.

				$U = U_{adv}$					$U = U_{adv} + U_{self}$				
	Δt (h)	V'_{azi} (cm s^{-1})	U_{adv} (cm s^{-1})	U (cm s^{-1})	R' (km)	T' (days)	r/R	R_o	U (cm s^{-1})	R' (km)	T' (days)	r/R	R_o
Mean	18	28.2	10.4	10.4	6.4	1.8	0.4	0.43	16.8	10.6	3.0	0.5	0.26
SD	9	9.4	3.2	3.2	3.0	1.0	0.2	0.27	3.4	4.7	1.6	0.2	0.16

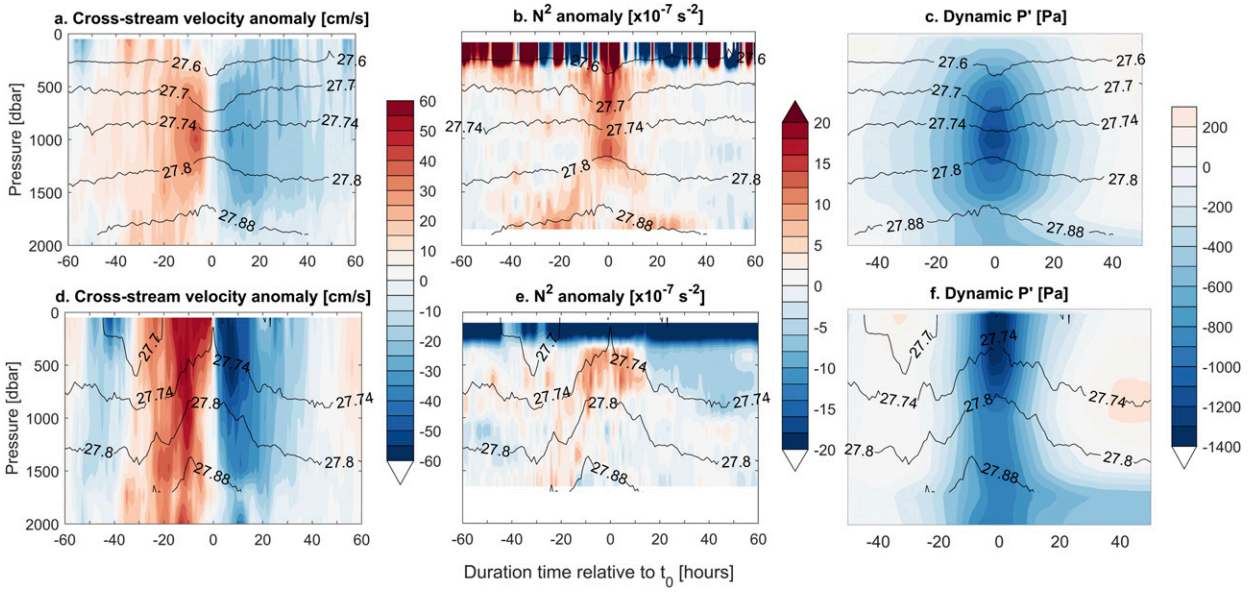

FIG. 13. Hourly time series of the (a) cross-stream velocity anomalies, (b) N^2 anomalies, and (c) dynamic pressure for an intermediate-layer intensified eddy that passed by mooring M1 on 19 Aug 2014. (d)–(f) As in (a)–(c), but for a near-surface intensified eddy that passed by M1 on 7 Mar 2015. Negative (positive) duration time indicates the hours before (after) the arrival of the apparent eddy center at t_0. The anomalies are relative to the monthly mean background profiles.

depth of strongest rotation (Figs. 13c,f). The intermediate-intensified cyclone has a minimum p at middepth and negligible p near the surface, indicating that this cyclone does not have a significant surface expression (Fig. 13c). On the other hand, the near-surface intensified cyclone has its minimum p at the surface, which is −1600 Pa and corresponds to a sea surface depression of 16 cm (Fig. 13f).

It is not clear whether the surface-intensified cyclones are DSOCs. They are found to be concentrated in winter–spring seasons based on 4-yr records at M1 (Fig. 12), raising the possibility that they may be DSOCs modified by convective waters from the interior Irminger Sea (Pickart et al. 2003; Le Bras et al. 2020). It is also possible that they are formed by a different mechanism, such as baroclinic instability of the boundary current along the East Greenland slope. Another possibility is that the DSOC is overlaid by an upper-layer convective cyclone, and they somehow manage to propagate in phase. The exact evolution of the cyclone's vertical structure awaits further investigation.

5. Discussion

a. Methodological aspects

A common approach to observe oceanic eddies and their trajectories is through satellite measurements. However, the satellite data are not as helpful for the DSOCs as for some other types of eddies. First, many DSOCs have intensified rotation at middepth and do not have a significant expression in sea surface height. Additionally, von Appen et al. (2014) attempted to investigate the sea surface temperature signatures associated with the DSOCs southwest of Denmark Strait but failed to establish a consistent relationship, suggesting that the sea surface temperature anomalies are likely associated with other processes. Finally, the DSOCs are quite small (radii of ~10 km) so that detecting them in standard gridded altimetry products is nearly impossible (Pujol et al. 2016). Even the higher-resolution along-track altimetry data are limited and noisy, both temporally and spatially, precluding a robust detection of the DSOCs. For example, the weak surface depression associated with the subsurface-intensified DSOCs cannot be easily distinguished from that induced by other types of variability, including surface-trapped eddies and variability of the boundary current itself.

The RAFOS floats, on the other hand, provide continuous high-resolution tracking of subsurface and small-scale eddy motions, which is particularly valuable for studying the fast-propagating DSOCs. Combined with hydrographic section and moorings, we have been able to provide a more thorough depiction of these cyclones.

b. Comparison of DSOCs with other submesoscale coherent vortices

The small size of the DSOCs (compared to the first internal deformation radius of ~15 km) and their subsurface-intensified velocity structure suggest that they could potentially be categorized as submesoscale coherent vortices (SCVs; McWilliams 2016). However, one distinct feature of the DSOCs compared to the other observed SCVs, such as the California Undercurrent eddy (e.g., Steinberg et al. 2019), the Mediterranean Water eddy (e.g., McDowell and Rossby 1978; Prater and Sanford 1994), and the Labrador Sea convective eddies (Lilly and Rhines 2002), is that their vertical length scales are comparable to the ocean depth, whereas most of the SCVs have more limited vertical

scales. This is likely attributed to the overall weakly stratified environment of the subpolar region such that rotations of the DSOCs can extend toward the ocean surface/bottom more easily. In addition, the DSOCs are cyclonic while most of the observed SCVs are anticyclonic. This is simply because the creation mechanism for DSOCs, i.e., vortex stretching, results in cyclones. The other group of deep-reaching cyclonic SCVs is recently observed in the northwestern Mediterranean Sea, and they are found to be produced by bottom-reaching convection in winters (Bosse et al. 2016).

c. Uncertainties of self-propagating speed of the DSOCs

In this study, the DSOC self-propagating speed is estimated as the Nof speed. However, it remains questionable whether the Nof solution is suitable for studying DSOCs. Specifically, the Nof solution is formulated for the propagation of a cold bottom lens whose overlying layer is sufficiently deep compared to the thickness of the blob or that the interaction between the blob and the overlying layer is weak. These conditions are apparently not satisfied for the DSOC observed at the CTD section. In addition, the Nof solution neglects friction, which might result in an overestimation of the self-propagating speed (Swaters and Flierl 1991).

Other studies suggest that the self-propagating speed of DSOCs southwest of the Denmark Strait is comparable to the phase speed of long topographic Rossby waves (Krauss and Käse 1998; von Appen et al. 2014). The latter is calculated as

$$c_{\text{Rossby}} = -\beta_T L_R^2, \tag{12}$$

where β_T is topographic β and is calculated as $\beta_T = -(f/H_0)\alpha$, where f is the Coriolis parameter, α is topographic slope, and H_0 is water depth; L_R is the first baroclinic Rossby deformation radius and is calculated as $L_R = NH_0/f$, where N is the depth-averaged background stratification. At the CTD section, $\beta_T = -5.2 \times 10^{-10}\,\text{m}^{-1}\,\text{s}^{-1}$, $\alpha = 0.008$, $H_0 = 1800$ m, and $L_R = 14$ km, where N approximated as $10^{-3}\,\text{s}^{-1}$. The resultant phase speed c_{Rossby} is $10.3\,\text{cm}\,\text{s}^{-1}$, which is larger than, but still comparable to, U_{self} ($7.5\,\text{cm}\,\text{s}^{-1}$) derived from observations. However, as pointed out in Krauss and Käse (1998), the nonlinearity of the eddies, indicated by the high Rossby number, precludes the rationale of using linear Rossby wave theory. In addition, McWilliams and Flierl (1979) have argued that the linear wave speed appears to be the fastest limit for the propagation speed of an isolated nonlinear vortex. Therefore, while the above analytical solutions may be used to approximate the DSOC propagating speed, they are not adequate to describe the dynamics of the cyclone.

d. Leakage of DSOCs into the basin interior

The observed DSOCs do not consistently follow the boundary around Cape Farewell. One of the key locations where the cyclones "leak" into the basin interior is at the southwestern corner of the Eirik Ridge, as indicated by several RAFOS floats whose trajectories showed cyclonic loops when they approached the southwestern corner of the Eirik Ridge along the 3000-m isobath. Instead of continuing along the same isobath and rounding the end of the ridge, the floats drifted off the 3000-m isobath into the basin interior (Fig. 5a). This is not surprising because the curvature of the 3000-m isobath is large enough (the radius is ~6 km) so that centrifugal force exceeds Coriolis force, possibly allowing separation to occur (Klinger 1994). Another possibility is that the cyclones are carried into the central Irminger Sea by retroflecting branches of the boundary current (Holliday et al. 2007). The loss of DSOCs around Eirik Ridge is consistent with mooring observations that compare cyclone occurrences between the east and west sides of Cape Farewell (Pacini et al. 2021).

There are other locations at both sides of Greenland where looping floats detached from the boundary current, but these events seem to be more random (Fig. 5a). Taken together, these float observations suggest that offshore transport of the overflow waters takes place around Greenland and the DSOCs may be an important agent for this transport to occur.

e. Potential spindown of the DSOCs

Previous studies have suggested that neutrally stable cyclonic SCVs tend to have a common Burger number of ~0.5 (McWilliams and Gent 1986). The Burger number is calculated as $B_r = [NH/(fL)]^2$, where N is the background stratification and H (L) is the vertical (horizontal) length scale of the cyclone. For the DSOCs at the OSNAP-East section, we take $N = 10^{-3}\,\text{s}^{-1}$, $H = 1800$ m, and $L = 10$ km. The resultant B_r is as large as 2.0, implying that the DSOCs may be barotropically unstable and subject to vertical segmentation into two eddies of smaller vertical scales and therefore more moderate B_r.

In addition to potential fragmentation, the DSOCs may also spin down along their propagation pathways as a result of friction, dissipation induced by vertical velocity shear, wave radiation (McWilliams and Flierl 1979; McWilliams and Gent 1986), and/or straining deformation (Graves et al. 2006). It remains a question of when and where the spindown takes place.

f. Comparison of current study with previous studies

The potential for DSOCs to trap fluid suggested in this study, however, appears to contrast with previous observations further upstream, southwest of the Denmark Strait at 65.5°N, which showed that the DSOCs were not able to trap fluid because of the swifter translational speed ($72\,\text{cm}\,\text{s}^{-1}$ with U_{adv} as $27\,\text{cm}\,\text{s}^{-1}$ and U_{self} as $45\,\text{cm}\,\text{s}^{-1}$) compared to V_{azi} ($22\,\text{cm}\,\text{s}^{-1}$; von Appen et al. 2014). A possible explanation is that the advective speed of the boundary current decreases southward from the Denmark Strait until a point, where the velocity difference between advection and self-propagation is small enough for the cyclones to start trapping fluid. The trapping is more efficient at middepth where azimuthal velocity is faster.

Additionally, we note the discrepancy between the abundant cyclonic rotations reported in this study and a previous study by Bacon and Saunders (2010), who found no predominance for cyclonic rotation in the deep layer according to a mooring array at southeastern Cape Farewell. One possible explanation is that the cyclone occurrences may exhibit significant interannual–decadal variability such that the different time periods between the two studies [2014–18 for current study and 2005/06 for Bacon and Saunders (2010)] lead to the discrepancy. Other possible attributions may include the different eddy identification methodologies used between the studies, which we do not discuss further.

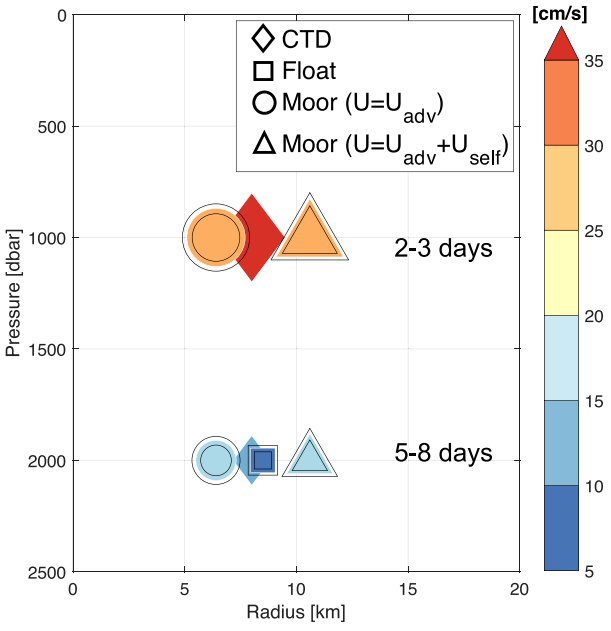

FIG. 14. A schematic summarizing the DSOC characteristics derived from different datasets. Diamonds/square represent results from CTD/floats. Two sets of mooring results are presented: circles indicate results with translational velocity approximated as advection only; and triangles denote results that consider both advection and self-propagation. Color and size of each marker denote the magnitude of mean azimuthal velocity as a function of pressure (1000 and 2000 dbar) and radius. The mean ± SD based on mooring and floats are plotted in black open markers. The derived rotational period at each pressure level is also labeled.

6. Summary

Using a RAFOS float dataset, a hydrographic transect and moorings, we have observed frequent passages of cyclonic eddies around southern Greenland during 2014–18. Characteristics of the cyclones derived from different datasets are summarized in Fig. 14. They are characterized by small radii (~10 km) and intense rotations at middepths (700–1000 dbar). The azimuthal velocities associated with the middepth cores are ~30 cm s^{-1} and the rotational periods are 2–3 days. In the underlying overflow water layer, the cyclonic rotations are still present, albeit much weaker. The azimuthal velocities are ~10 cm s^{-1} and the rotational periods are about 5–8 days. From a kinematic point of view, the strong middepth rotation offers the potential for the cyclones to trap fluid and transport it downstream. The cyclones contain positive potential vorticity anomalies within the rotation cores and are shown to introduce cold, fresh, and dense anomalies to the overflow water layer of the boundary current. These observed characteristics of the cyclones suggest that they are likely Denmark Strait overflow cyclones (DSOCs), which are formed by vortex stretching south of the sill and propagate along the boundary currents around Greenland.

In addition to introducing property anomalies, a recent study has shown that the presence of DSOCs leads to an increased transport of Denmark Strait Overflow Water west of Cape Farewell by 23% according to mooring observations (Pacini et al. 2021). Taken together, the DSOCs are at least partially responsible for the property and transport variabilities of the deep boundary currents around southern Greenland that were observed by previous studies (Fischer et al. 2015; Bacon and Saunders 2010). Another potential influence of DSOCs is on the stability of the boundary currents and therefore the shedding of eddies, which is essential for boundary–interior exchange (Le Bras et al. 2020; Eden and Böning 2002; de Jong et al. 2014). All of these processes are critical aspects to improve model representation of mixing, ventilation, and circulation characteristics in the subpolar North Atlantic (Danabasoglu et al. 2014; Wang et al. 2015).

Acknowledgments. The authors wish to thank the personnel, crew, and technicians of the R/V *Knorr*, R/V *Thalassa*, CCGS *Hudson*, R/V *Pelagia*, R/V *Discovery*, R/V *MSMerian*, and R/V *Armstrong*, for their efforts deploying and recovering the sound source moorings, deploying the RAFOS floats, as well as collecting the CTD data used in this study. Gratitude is extended to the OSNAP group for collecting, calibrating, and processing the mooring data. OOI mooring data are based upon work supported by the National Science Foundation under Cooperative Agreement 1743430. S. Zou, A. Bower, and H. Furey gratefully acknowledge the support from the Physical Oceanography Program of the U.S. National Science Foundation Grant OCE-1756361. R.S. Pickart acknowledges support from National Science Foundation Grants OCE-1259618 and OCE-1756361. N. P. Holliday and L. Houpert were supported by NERC programs U.K. OSNAP (NE/K010875) and U.K. OSNAP-Decade (NE/T00858X/1). S. Zou also acknowledges the following individuals for their contributions to this work: L. Pratt and I. Rypina for their comments and feedback; P. Lin for the ship-mounted ADCP data; A. Pacini for sharing the detiding code; and N. Foukal for sharing the data interpolation code.

Data availability statement. RAFOS float data can be accessed at Woods Hole Open Access Server (https://doi.org/10.26025/1912/24388). OSNAP products, CTD and mooring data can be accessed at www.o-snap.org. The data were collected and made freely available by the OSNAP project and all the national programs that contribute to it.

REFERENCES

Almansi, M., T. W. N. Haine, R. Gelderloos, and R. S. Pickart, 2020: Evolution of Denmark Strait overflow cyclones and their relationship to overflow surges. *Geophys. Res. Lett.*, **47**, e2019GL086759, https://doi.org/10.1029/2019GL086759.

Armi, L., D. Hebert, N. Oakey, J. F. Price, P. L. Richardson, H. T. Rossby, and B. Ruddick, 1989: Two years in the life of a Mediterranean salt lens. *J. Phys. Oceanogr.*, **19**, 354–370, https://doi.org/10.1175/1520-0485(1989)019<0354:TYITLO>2.0.CO;2.

Bacon, S., and P. M. Saunders, 2010: The deep western boundary current at Cape Farewell: Results from a moored current meter array. *J. Phys. Oceanogr.*, **40**, 815–829, https://doi.org/10.1175/2009JPO4091.1.

Bosse, A., and Coauthors, 2016: Scales and dynamics of submesoscale coherent vortices formed by deep convection in the northwestern Mediterranean Sea. *J. Geophys. Res. Oceans*, **121**, 7716–7742, https://doi.org/10.1002/2016JC012144.

Bruce, J. G., 1995: Eddies southwest of the Denmark Strait. *Deep-Sea Res. I*, **42**, 13–29, https://doi.org/10.1016/0967-0637(94)00040-Y.

Danabasoglu, G., and Coauthors, 2014: North Atlantic simulations in Coordinated Ocean-ice Reference Experiments phase II (CORE-II). Part I: Mean states. *Ocean Modell.*, **73**, 76–107, https://doi.org/10.1016/j.ocemod.2013.10.005.

de Jong, M. F., A. S. Bower, and H. H. Furey, 2014: Two years of observations of warm-core anticyclones in the Labrador Sea and their seasonal cycle in heat and salt stratification. *J. Phys. Oceanogr.*, **44**, 427–444, https://doi.org/10.1175/JPO-D-13-070.1.

Dickson, R. R., and J. Brown, 1994: The production of North Atlantic Deep Water: Sources, rates, and pathways. *J. Geophys. Res.*, **99**, 12 319–12 341, https://doi.org/10.1029/94JC00530.

——, and Coauthors, 2008: The overflow flux west of Iceland: Variability origin and forcing. *Arctic–Subarctic Ocean Fluxes*, R. R. Dickson, J. Meincke, and P. Rhines, Eds., Springer, 443–474.

Eden, C., and C. Böning, 2002: Sources of eddy kinetic energy in the Labrador Sea. *J. Phys. Oceanogr.*, **32**, 3346–3363, https://doi.org/10.1175/1520-0485(2002)032<3346:SOEKEI>2.0.CO;2.

Egbert, G. D., and S. Y. Erofeeva, 2002: Efficient inverse modeling of barotropic ocean tides. *J. Atmos. Oceanic Technol.*, **19**, 183–204, https://doi.org/10.1175/1520-0426(2002)019<0183:EIMOBO>2.0.CO;2.

Fischer, J., and Coauthors, 2015: Intra-seasonal variability of the DWBC in the western subpolar North Atlantic. *Prog. Oceanogr.*, **132**, 233–249, https://doi.org/10.1016/j.pocean.2014.04.002.

Flierl, G. R., 1981: Particle motions in large-amplitude wave fields. *Geophys. Astrophys. Fluid Dyn.*, **18**, 39–74, https://doi.org/10.1080/03091928108208773.

Girton, J. B., and T. B. Sanford, 2003: Descent and modification of the overflow plume in the Denmark Strait. *J. Phys. Oceanogr.*, **33**, 1351–1364, https://doi.org/10.1175/1520-0485(2003)033<1351:DAMOTO>2.0.CO;2.

Graves, L. P., J. C. McWilliams, and M. T. Montgomery, 2006: Vortex evolution due to straining: A mechanism for dominance of strong, interior anticyclones. *Geophys. Astrophys. Fluid Dyn.*, **100**, 151–183, https://doi.org/10.1080/03091920600792041.

Hill, A. E., 1996: Spin-down and the dynamics of dense pool gyres in shallow seas. *J. Mar. Res.*, **54**, 471–486, https://doi.org/10.1357/0022240963213538.

Holliday, N. P., A. Meyer, S. Bacon, S. G. Alderson, and B. de Cuevas, 2007: Retroflection of part of the east Greenland current at Cape Farewell. *Geophys. Res. Lett.*, **34**, L07609, https://doi.org/10.1029/2006GL029085.

Hopkins, J. E., N. P. Holliday, D. Rayner, L. Houpert, I. Le Bras, F. Straneo, C. Wilson, and S. Bacon, 2019: Transport variability of the Irminger Sea Deep Western Boundary Current from a mooring array. *J. Geophys. Res. Oceans*, **124**, 3246–3278, https://doi.org/10.1029/2018JC014730.

Jiang, L., and R. W. Garwood Jr., 1996: Three-dimensional simulations of overflows on continental slopes. *J. Phys. Oceanogr.*, **26**, 1214–1233, https://doi.org/10.1175/1520-0485(1996)026<1214:TDSOOO>2.0.CO;2.

Jungclaus, J. H., J. Hauser, and R. H. Käse, 2001: Cyclogenesis in the Denmark Strait overflow plume. *J. Phys. Oceanogr.*, **31**, 3214–3229, https://doi.org/10.1175/1520-0485(2001)031<3214:CITDSO>2.0.CO;2.

Käse, R. H., J. B. Girton, and T. B. Sanford, 2003: Structure and variability of the Denmark Strait Overflow: Model and observations. *J. Geophys. Res. Oceans*, **108**, 3181, https://doi.org/10.1029/2002JC001548.

Klinger, B. A., 1994: Inviscid current separation from rounded capes. *J. Phys. Oceanogr.*, **24**, 1805–1811, https://doi.org/10.1175/1520-0485(1994)024<1805:ICSFRC>2.0.CO;2.

Koszalka, I. M., T. W. N. Haine, and M. G. Magaldi, 2017: Mesoscale mixing of the Denmark Strait Overflow in the Irminger basin. *Ocean Modell.*, **112**, 90–98, https://doi.org/10.1016/j.ocemod.2017.03.001.

Krauss, W., 1996: A note on overflow eddies. *Deep-Sea Res. I*, **43**, 1661–1667, https://doi.org/10.1016/S0967-0637(96)00073-8.

——, and R. H. Käse, 1998: Eddy formation in the Denmark Strait overflow. *J. Geophys. Res. Oceans*, **103**, 15 525–15 538, https://doi.org/10.1029/98JC00785.

Lauderdale, J. M., S. Bacon, A. C. Naveira Garabato, and N. P. Holliday, 2008: Intensified turbulent mixing in the boundary current system of southern Greenland. *Geophys. Res. Lett.*, **35**, L04611, https://doi.org/10.1029/2007GL032785.

Le Bras, I. A.-A., F. Straneo, J. Holte, M. F. de Jong, and N. P. Holliday, 2020: Rapid export of waters formed by convection near the Irminger Sea's western boundary. *Geophys. Res. Lett.*, **47**, e2019GL085989, https://doi.org/10.1029/2019GL085989.

Lilly, J. M., and P. B. Rhines, 2002: Coherent eddies in the Labrador Sea observed from a mooring. *J. Phys. Oceanogr.*, **32**, 585–598, https://doi.org/10.1175/1520-0485(2002)032<0585:CEITLS>2.0.CO;2.

Lin, P., R. S. Pickart, D. J. Torres, and A. Pacini, 2018: Evolution of the freshwater coastal current at the southern tip of Greenland. *J. Phys. Oceanogr.*, **48**, 2127–2140, https://doi.org/10.1175/JPO-D-18-0035.1.

——, ——, K. Jochumsen, G. W. K. Moore, H. Valdimarsson, T. Fristedt, and L. J. Pratt, 2020: Kinematic structure and dynamics of the Denmark Strait overflow from ship-based observations. *J. Phys. Oceanogr.*, **50**, 3235–3251, https://doi.org/10.1175/JPO-D-20-0095.1.

Lozier, M. S., and Coauthors, 2017: Overturning in the Subpolar North Atlantic Program: A new international ocean observing system. *Bull. Amer. Meteor. Soc.*, **98**, 737–752, https://doi.org/10.1175/BAMS-D-16-0057.1.

——, and Coauthors, 2019: A sea change in our view of overturning in the subpolar North Atlantic. *Science*, **363**, 516–521, https://doi.org/10.1126/science.aau6592.

Magaldi, M. G., T. W. Haine, and R. S. Pickart, 2011: On the nature and variability of the East Greenland Spill Jet: A case study in summer 2003. *J. Phys. Oceanogr.*, **41**, 2307–2327, https://doi.org/10.1175/JPO-D-10-05004.1.

McDowell, S. E., and H. T. Rossby, 1978: Mediterranean water: An intense mesoscale eddy off the Bahamas. *Science*, **202**, 1085–1087, https://doi.org/10.1126/science.202.4372.1085.

McWilliams, J. C., 2016: Submesoscale currents in the ocean. *Proc. Roy. Soc.*, **A472**, 20160117, https://doi.org/10.1098/rspa.2016.0117.

——, and G. R. Flierl, 1979: On the evolution of isolated, nonlinear vortices. *J. Phys. Oceanogr.*, **9**, 1155–1182, https://doi.org/10.1175/1520-0485(1979)009<1155:OTEOIN>2.0.CO;2.

——, and P. R. Gent, 1986: The evolution of sub-mesoscale, coherent vortices on the β-plane. *Geophys. Astrophys. Fluid Dyn.*, **35**, 235–255, https://doi.org/10.1080/03091928608245894.

Nof, D., 1983: The translation of isolated cold eddies on a sloping bottom. *Deep-Sea Res.*, **30A**, 171–182, https://doi.org/10.1016/0198-0149(83)90067-5.

North, R. P., K. Jochumsen, and M. Moritz, 2018: Entrainment and energy transfer variability along the descending path of the

Denmark Strait overflow plume. *J. Geophys. Res. Oceans*, **123**, 2795–2807, https://doi.org/10.1002/2018JC013821.

OOI, 2020: NSF Ocean Observatories Initiative Data Portal. Accessed 27 January, http://ooinet.oceanobservatories.org.

Pacini, A., and Coauthors, 2020: Mean conditions and seasonality of the West Greenland boundary current system near Cape Farewell. *J. Phys. Oceanogr.*, **50**, 2849–2871, https://doi.org/10.1175/JPO-D-20-0086.1.

——, R. S. Pickart, I. A. Le Bras, F. Straneo, and N. P. Holliday, 2021: Cyclonic eddies in the West Greenland boundary current system. *J. Phys. Oceanogr.*, **51**, 2087–2102, https://doi.org/10.1175/JPO-D-20-0255.1.

Pawlowicz, R., B. Beardsley, and S. Lentz, 2002: Classical tidal harmonic analysis including error estimates in MATLAB using T_TIDE. *Comput. Geosci.*, **28**, 929–937, https://doi.org/10.1016/S0098-3004(02)00013-4.

Pickart, R. S., M. A. Spall, M. H. Ribergaard, G. K. Moore, and R. F. Milliff, 2003: Deep convection in the Irminger Sea forced by the Greenland tip jet. *Nature*, **424**, 152–156, https://doi.org/10.1038/nature01729.

Prater, M. D., and T. B. Sanford, 1994: A meddy off Cape St. Vincent. Part I: Description. *J. Phys. Oceanogr.*, **24**, 1572–1586, https://doi.org/10.1175/1520-0485(1994)024<1572:AMOCSV>2.0.CO;2.

Price, J. F., and M. O. N. Baringer, 1994: Outflows and deep water production by marginal seas. *Prog. Oceanogr.*, **33**, 161–200, https://doi.org/10.1016/0079-6611(94)90027-2.

Pujol, M. I., Y. Faugère, G. Taburet, S. Dupuy, C. Pelloquin, M. Ablain, and N. Picot, 2016: DUACS DT2014: The new multi-mission altimeter data set reprocessed over 20 years. *Ocean Sci.*, **12**, 1067–1090, https://doi.org/10.5194/os-12-1067-2016.

Ramsey, A., H. Furey, and A. Bower, 2020: Overturning of the Subpolar North Atlantic Program (OSNAP): RAFOS Float Data Report, June 2014–January 2019. Woods Hole Oceanographic Institution Tech. Rep. WHOI-2020-06, 508 pp., https://doi.org/10.1575/1912/26515.

Regier, L., and H. Stommel, 1979: Float trajectories in simple kinematic flows. *Proc. Natl. Acad. Sci. USA*, **76**, 4760–4764, https://doi.org/10.1073/pnas.76.10.4760.

Richardson, P. L., J. F. Price, D. Walsh, L. Armi, and M. Schröder, 1989: Tracking three meddies with SOFAR floats. *J. Phys. Oceanogr.*, **19**, 371–383, https://doi.org/10.1175/1520-0485(1989)019<0371:TTMWSF>2.0.CO;2.

Ross, C. K., 1982: Overflow '73—Denmark Strait: Vol 3—Temperature, salinity and sigma-t sections. Canadian Tech. Rep. of Hydrography and Ocean Sciences 16, Bedford Institute of Oceanography, Dartmouth, NS, Canada, 57 pp., https://publications.gc.ca/collections/collection_2015/mpo-dfo/Fs97-18-16-eng.pdf.

Rossby, T., D. Dorson, and J. Fontaine, 1986: The RAFOS system. *J. Atmos. Oceanic Technol.*, **3**, 672–679, https://doi.org/10.1175/1520-0426(1986)003<0672:TRS>2.0.CO;2.

Rudels, B., E. Fahrbach, J. Meincke, G. Budéus, and P. Eriksson, 2002: The East Greenland Current and its contribution to the Denmark Strait overflow. *ICES J. Mar. Sci.*, **59**, 1133–1154, https://doi.org/10.1006/jmsc.2002.1284.

Schaffer, J., T. Kanzow, K. Jochumsen, K. Lackschewitz, S. Tippenhauer, V. M. Zhurbas, and D. Quadfasel, 2016: Enhanced turbulence driven by mesoscale motions and flow-topography interaction in the Denmark Strait Overflow plume. *J. Geophys. Res. Oceans*, **121**, 7650–7672, https://doi.org/10.1002/2016JC011653.

Smith, P. C., 1976: Baroclinic instability in the Denmark Strait overflow. *J. Phys. Oceanogr.*, **6**, 355–371, https://doi.org/10.1175/1520-0485(1976)006<0355:BIITDS>2.0.CO;2.

Spall, M. A., and J. F. Price, 1998: Mesoscale variability in Denmark Strait: The PV outflow hypothesis. *J. Phys. Oceanogr.*, **28**, 1598–1623, https://doi.org/10.1175/1520-0485(1998)028<1598:MVIDST>2.0.CO;2.

——, R. S. Pickart, P. Lin, W. J. von Appen, D. Mastropole, H. Valdimarsson, T. W. Haine, and M. Almansi, 2019: Frontogenesis and variability in Denmark Strait and its influence on overflow water. *J. Phys. Oceanogr.*, **49**, 1889–1904, https://doi.org/10.1175/JPO-D-19-0053.1.

Steinberg, J. M., N. A. Pelland, and C. C. Eriksen, 2019: Observed evolution of a California Undercurrent eddy. *J. Phys. Oceanogr.*, **49**, 649–674, https://doi.org/10.1175/JPO-D-18-0033.1.

Swaters, G. E., 1991: On the baroclinic instability of cold-core coupled density fronts on a sloping continental shelf. *J. Fluid Mech.*, **224**, 361–382, https://doi.org/10.1017/S0022112091001799.

——, and G. R. Flierl, 1991: Dynamics of ventilated coherent cold eddies on a sloping bottom. *J. Fluid Mech.*, **223**, 565–587, https://doi.org/10.1017/S0022112091001556.

Voet, G., and D. Quadfasel, 2010: Entrainment in the Denmark Strait overflow plume by meso-scale eddies. *Ocean Sci.*, **6**, 301–310, https://doi.org/10.5194/os-6-301-2010.

von Appen, W. J., R. S. Pickart, K. H. Brink, and T. W. Haine, 2014: Water column structure and statistics of Denmark Strait Overflow Water cyclones. *Deep-Sea Res. I*, **84**, 110–126, https://doi.org/10.1016/j.dsr.2013.10.007.

——, D. Mastropole, R. S. Pickart, H. Valdimarsson, S. Jónsson, and J. B. Girton, 2017: On the nature of the mesoscale variability in Denmark Strait. *J. Phys. Oceanogr.*, **47**, 567–582, https://doi.org/10.1175/JPO-D-16-0127.1.

Wang, H., S. A. Legg, and R. W. Hallberg, 2015: Representations of the Nordic Seas overflows and their large scale climate impact in coupled models. *Ocean Modell.*, **86**, 76–92, https://doi.org/10.1016/j.ocemod.2014.12.005.

Whitehead, J. A., M. E. Stern, G. R. Flierl, and B. A. Klinger, 1990: Experimental observations of baroclinic eddies on a sloping bottom. *J. Geophys. Res. Oceans*, **95**, 9585–9610, https://doi.org/10.1029/JC095iC06p09585.